LAWRENCE
LIVERMORE
NATIONAL
LABORATORY

LLNL-JRNL-842205

Control of low-mode drive asymmetry in an efficient long pulse low-density filled hohlraum

N. IZUMI, T. Doeppner, J. Milovich, O. L. Landen, D. A. Callahan, T. Chapman, D. E. Hinkel, C. V. Houldin Hatala, S. Khan, J. J. Kroll, B. J. MacGowan, D. Mariscal, M. Millot, J. D. Moody, K. Newman, R. Ross, E. Tubman, S. Vonhof

November 8, 2022

Physics of Plasmas

Disclaimer

This document was prepared as an account of work sponsored by an agency of the United States government. Neither the United States government nor Lawrence Livermore National Security, LLC, nor any of their employees makes any warranty, expressed or implied, or assumes any legal liability or responsibility for the accuracy, completeness, or usefulness of any information, apparatus, product, or process disclosed, or represents that its use would not infringe privately owned rights. Reference herein to any specific commercial product, process, or service by trade name, trademark, manufacturer, or otherwise does not necessarily constitute or imply its endorsement, recommendation, or favoring by the United States government or Lawrence Livermore National Security, LLC. The views and opinions of authors expressed herein do not necessarily state or reflect those of the United States government or Lawrence Livermore National Security, LLC, and shall not be used for advertising or product endorsement purposes.

Control of low-mode drive asymmetry in an efficient long pulse low-density filled hohlraum

N. Izumi[1], T. Döppner[1], J. L. Milovich[1], O. L. Landen[1], D. A. Callahan[1], T. Chapman[1], D. E. Hinkel[1], C.V. Houldin Hatala[1], S. Khan[1], J. J. Kroll[1], B. J. MacGowan[1], E. Marin[2], D. Mariscal[1], M. Mauldin[2], M. Millot[1], J. D. Moody[1], K. Newman[1], M. Ratledge[2] J. S. Ross[1], E. Tubman[1], S. Vonhof[2], J. Wall[2]

[1]Lawrence Livermore National Laboratory, Livermore, California 94550, USA

[2]General Atomics, La Jolla, California 92121, USA

Abstract

Laser-driven hohlraums filled with gas at lower densities (< 0.6 mg/cc) have higher efficiency compared to original ≥ 0.96 mg/cc fill because of reduced backscatter losses (G. Hall *et. al.*, Phys. Plasmas 24 (2017) 052706). However, using low density filled hohlraums with longer drive required for lower adiabat implosions, and hence potentially higher ICF gain designs, has been challenging since the hohlraum wall blow-off is less tamped thus altering the laser beam absorption regions and drive symmetry. A series of NIF experiments using optimized pulse shaping, beam pointing, and temporal phasing have demonstrated, through imaging of the hohlraum and capsule dynamics, that a symmetric implosion using a 14 ns low-adiabat drive pulse (2x longer than HDC ablator designs using low density fill hohlraums (L. Divol *et. al.*, Phys. Plasmas 24 (2017) 056309)) is possible in a low backscatter loss 0.45 mg/cc He-filled hohlraum. The ingress of the hohlraum walls was mitigated by revisiting the adiabat-shaped design (Clark *et. al.*, Phys. Plasmas 21 (2014) 112705) that uses a low power (1 TW) trough that delays the wall expansion. Low mode P_2 and P_4 drive asymmetry swings caused by the drift of the laser spots were essentially zeroed-out by employing temporal beam phasing between cones of beams (R. Turner *et. al*. Phys Plasmas 7 (2000) 333). The results also indicate an improved coupling efficiency of ~30% compared to an earlier design using higher density fill hohlraums and pave the way for revisiting low adiabat, high convergence drives using CH ablators.

LLNL-JRNL-842205

I. Introduction

A key element to a high performance inertial confinement fusion (ICF) implosion is the spherically symmetric acceleration and deceleration of the shell[1]. Kinetic energy gained by ablative acceleration of the spherical shell target is converted to internal energy during the deceleration phase of the implosion. Maximum volumetric compression of the fuel can be achieved only when the shell has purely radial momentum and synchronized radial trajectories. If the radial momentum over the surface is not uniform enough, non-radial motion sets in, the stagnation phase experiences asynchrony giving rise to non-uniform shell areal density, fuel and hot spot compression is lowered, and a significant fraction of the kinetic energy is not converted to internal energy[2-6].

In the case of indirectly driven ICF using a laser-driven hohlraum[7], drive asymmetries in higher spatial modes at the capsule surface due to the individual bright laser spots and the laser entrance holes (LEH) are smoothed out efficiently because of the geometric smoothing of radiation transport between the hohlraum wall and the capsule surface[8]. However, this smoothing is limited for lower mode perturbations (those with Legendre mode < 5). Therefore, control of low mode asymmetry at the hohlraum wall throughout the drive pulse length is important. Moreover, because of laser ablation of the hohlraum wall under the laser spots, the location of beam power deposition departs from the initial surface of the wall. This dynamic motion of the beam irradiation spot will change the symmetry of the soft X-ray drive on the capsule[9, 10].

Achieving high gain, requires high convergence to increase the burn rate[11, 12]. This in turn, dictates even tighter drive symmetry control. At NIF scale, it also requires a low adiabat implosion (convergence ~ $1/\sqrt{\alpha}$ where α, the adiabat, is defined as the ratio of the fuel pressure over the Fermi degenerate pressure), hence a low first shock pressure P_s. Current high-density-carbon (HDC) ablator designs require a minimum P_s (~12 MB) to melt its crystalline structure[13, 14] and avoid seeding hydro-dynamic instability growth, thus limiting the lowest achievable adiabat (~2). Amorphous CH ablators do not require such a strong 1st shock and hence merit another look. For an initial ablator density ρ_0 and thickness Δr_0, the first shock travel time in the ablator is~ $\Delta r_o/\sqrt{P_s/\rho_o}$. Per the rocket equation for indirect drive, for a given capsule radius, the ablator mass areal density ablated for ignition relevant peak implosion velocities is almost fixed (90-95% of $\rho_0\Delta r_0$), so the first shock travel time can be rewritten as scaling $1/\sqrt{P_s\rho_o}$. So, for the low adiabat CH designs, with both ρ_o and P_s 3 times lower than for HDC ablators, the first shock epoch is 3x longer and the total drive is ≈ 2x longer. This makes drive symmetry control in the face of hohlraum wall blow-in harder, which motivated the use of high He gas-fill (ρ_{He} = 0.96 mg/cc) in the first NIF low adiabat CH designs[15, 16] to tamp the hohlraum wall plasma. A later[17] CH design that improved performance by intentionally reducing compression to reduce hydrodynamic instability growth[18] used a higher picket and shorter trough requiring even higher gas-fill (1.6 mg/cc). Both low and high adiabat designs suffered from large (20%) backscatter losses (SBS and SRS also creating hot electrons) and impaired inner beam propagation[19] to the hohlraum equatorial region where hohlraum fill densities reached > 10% n_{crit}(critical density) late in time as capsule ablation and wall blow-off squeezed the He gas. Large amounts of cross

beam energy transfer[20] (CBET) were needed to recover P_2 (pole versus equator) drive symmetry, but that in itself could not fix time-dependent asymmetry excursions.

A switch to HDC capsules requiring shorter drive pulses allowed the tamping gas density to be reduced to 0.3 mg/cc, dropping LPI backscatter losses to a few percent (~< 5%) levels[21, 22]. At present, the maximum pulse length is limited by the ingress of the wall plasma from the outer beam spots clipping the inner beams before they reach the hohlraum midplane[23, 24]. Furthermore, the shorter laser pulses minimize the outer beam spots backward motion as the wall blows in which leads to a changing drive asymmetry at the capsule[9]. The question that is being revisited here is, can we use the advantages and circumvent the disadvantages of a lower backscatter loss, low gas-fill hohlraum for the low adiabat long pulse CH designs?

In this paper, we discuss the strategies that experimentally did or did not work (and provide some physical reasons) on the path to demonstrate time-dependent symmetry control of a long pulse design in a low-density filled hohlraum. The main components of the strategy were: applying temporal beam power phasing, both in polar and azimuthal directions, using a low power trough design after first shock launch, and ultimately cross beam energy transfer (CBET). Section II explains and presents the experimental strategy, parameters, and measurement techniques. The results of the time-dependent hohlraum and capsule dynamics are presented in Section III. In Section IV, we summarize by discussing the efficiency gains by comparing to high gas-fill and prior low gas-fill designs and discuss extrapolations to larger scale.

II. Experimental Design

A. Strategy

The first major concern for drive symmetry control is the laser spot motion[9]. The outer laser spots by virtue of being outward and having 2x steeper incidence angle and hence higher turning point density ≈ $\sin^2\theta$ (where θ is the angle of the beam propagation direction relative to the hohlraum axis) are not substantially impeded by hot coronal plasma blow-off. However, their energy deposition regions do move back along their incident path due to the x-ray induced wall ablation at high (> critical) density. For a given x-ray drive ~ $T_r^4 t$, the angular motion of the energy deposition spot due to mass ablation of the wall ($m \sim T_r^{1.8} t$) scales as m/R hence as $\sqrt{t}$/R (larger for longer pulses of length t and smaller hohlraums of radius R). Such angular spot motion if unchecked will preclude (by geometry) zeroing out the P_2 and P_4 drive asymmetries sufficiently at all time solely by using 2 cones of beams per side[7].

To reduce this spot motion driven symmetry swing, we stagger in time the onset of outer beams pointed at different locations, a technique previously demonstrated on Nova 10 beam implosions split into 2 halves per beam[25] and Omega 40 beam implosions[26]. The NIF[27] is particularly well suited for this since the outer beams/side are split into 8 interleaved quads each at 44.5° and 50° that naturally irradiate a cylindrical hohlraum wall at different axial distances as shown in Fig. 2b. This effectively splits up the illumination into more than 2 cones per side. As shown in Fig. 2a, at the start of the picket, only the 50° irradiate the hohlraum wall nearest the LEH end (largest axial location z). After the foot pulse, once the wall and hence the spot motion of the 50° becomes significant, the 44.5° quads that are pointed closer to

the capsule side are turned on as shown in Fig. 2d. In this way, as illustrated in Fig. 2b, the centroid angle subtended at the capsule by the outer spots can be reset to what it was earlier in the pulse thus compensating for the symmetry swing due to spot motion of individual outer cone beams.

The second concern for controlling drive symmetry for a long pulse drive in a low gas-fill hohlraum is the coronal plasma blow-off from the high-Z hohlraum walls impairing the inner beam propagation[23]. Specifically, the portion of the hohlraum wall (typically gold) irradiated by the outer cone beams expands the fastest and the hot gold plasma ablated off the wall begins to fill the volume initially occupied by the helium gas. This high-Z wall plasma "bubble" will eventually intersect the path of the inner cone beams as shown in Fig. 1. Additionally, due to the cylindrical convergent hohlraum geometry, the density of the bubble also increases further enhancing the absorption of the inner cone beams by inverse-bremsstrahlung[28].

An obvious strategy to avoid inner beam propagation impairment at a given hohlraum initial radius) and gas-fill density would be to reduce the initial capsule radius r_o and ablator thickness proportionately[29], thus reducing the required drive pulse length $\tau \sim r_o$ for a given desired implosion velocity. This approach has the additional advantage of increased geometric smoothing[30] at the capsule of any Legendre mode $l = 4$ asymmetry at the hohlraum wall by a factor $\sim(r_o/R)^2$. However, the smaller scale leads to a reduction of the maximum yield (Y), that scales (in the absence of alpha heating) as $\sim r_o^{4.4}$, all else equal[31], and the likelihood of ignition[11, 15, 32], where the Ignition Threshold Factor (ITFX ~ $Y(\rho r)^{2.1}/r_o^3$) scales as $r_o^{3.5}$ for final fuel areal density $\rho r \sim r_o$. So, a further strategy or strategies are required to maintain symmetry control without overly compromising coupling efficiency between hohlraum and capsule ~ $(r_o/R)^2$.

At NIF[27], each quad consists of 4 beams. By further splitting pairs of beams within each outer quad azimuthally by ± 400 μm, a standard procedure, the whole azimuth of a 5.75 mm diameter hohlraum is filled with laser illumination (Fig. 3a or b) for each of the 45° and 50° cones. Due to their smaller spots and being closer to normal incidence, the 50° quads have 25% more intense irradiation than the 45° and 13% higher areal mass ablation rate ~ $(\sin\theta)^{4/3}$ for fixed surface intensity[33], and hence dominate the outer bubble growth. This will be even truer when applying the temporal beam staggering discussed above. This suggests an alternate mitigation strategy, namely break up the 50° cone bubble annulus into 3D bubbles by delaying the onset of half of the 50° cone beams, a technique which we call hereafter "azimuthal beam phasing" (ABP). In the case here, 4 symmetrically distributed 50° quads per side are turned on during the foot of the pulse, as shown in Fig. 3c, denoted as 50a quads. Since those outer quads must have 4x the power of the case without temporal beam staggering or ABP (Fig. 2d) to keep the total power of the outer cones fixed, the laser peak power and energy limits per quad (of the NIF laser) set a limit on the duration for which the phasing can occur before all 50° beams must be turned on. For the work presented here, that was chosen after the foot and trough of the laser pulse. The net result is the formation of non-azimuthally symmetric plasma bubbles with gaps between them that should persist even after the remaining outer beams are turned on. This would, in principle, let every other inner beam propagate

relatively unimpaired, while those inner beams azimuthally in phase with these bubbles would be predicted to be intercepted earlier.

Consequently, one could ask what is the overall benefit of the azimuthal beam phasing? The potential advantage lies in the sublinear dependence of the laser areal mass ablation rates, which scales [7] as $I^{1/3}$, I being laser intensity. Hence, if all the 50° beam power is distributed in 8 instead of 16 outer quads, the irradiation intensity of the 8 quads has to be increased by factor 2 to keep the same x-ray drive, but the area of the irradiated wall goes down by factor 2. Then, the total 50° cone ablated mass during the foot should be reduced by a factor of $\frac{1}{2} \times 2^{1/3} = 2^{-2/3} = 0.6\text{x}$. However, when including the mass ablated during the peak of the pulse (~4x more ablated mass during the 3 ns peak drive with 10x higher intensity for the 50° quads), this fractional reduction will be substantially less. Furthermore, the uniform soft x-ray ablation of the high-Z walls will also contribute to the bubble motion, although less, since it is occurring at higher density. Still, even a 10% reduction in laser ablated mass could lengthen the duration of adequate inner beam propagation by a useful 0.4 ns.

The weak dependence of mass ablation rate and exhaust velocity to laser intensity (scaling as $I_{laser}^{1/3}$) and x-ray intensities ($T_r^{1.8}$ and $T_r^{0.7} \approx I_{xray}^{0.5}$ and $I_{xray}^{0.2}$ for high Z walls[34]) can explain why the outer bubble growth for pulse shapes with gently rising intensities after the initial picket has been measured as ballistic[23, 28]. By ballistic, we mean that their trajectory extrapolates linearly back to the start of outer beams for pulse profiles with modest (< 15x) intensity contrast between the foot and peak of the laser pulse. This realization suggested a second tactic, namely choose a design for which the trough power between foot and peak is significantly less. The 4-shock adiabat-shaped CH ablator design shown in Fig. 2c and d uses such a 5-10x lower trough power after a high picket to create a decaying shock[35-37], such that the ablator is on a high adiabat while the DT fuel experiences a weaker first shock and hence stays on a low adiabat. From a capsule perspective, this design provided minimal increase in adiabat[38, 39] over the original lower picket 4-shock design while mitigating ablation front instability growth[37, 40, 41], and showed a 4x increase in performance at high areal density[42, 43]. The approximation of a constant speed, hence ballistic bubble trajectory, that works well for pulses with continuously increasing drive[24, 28] should not be expected for such low trough outer pulses. A sufficiently low trough should temporarily lessen bubble growth by reducing the wall mass ablation rate since insufficient mass is supplied to the expanding bubble to push against the existing shocked hohlraum gas-fill. Such a temporary drop in bubble ingress speed should greatly increase the chances for maintaining inner beam propagation for the CH pulses whose pulse length is dominated by the trough section.

Existing symmetry control strategies can also be added, such as varying the wavelength separation between the inner and outer cones to change the cross beam energy transfer (CBET) between inners and outers[44] to reduce the average P_2 drive asymmetry. A judicious choice of initial outer beam pointing and hence hohlraum length is required to minimize the average P_4 asymmetry. A time-dependent ratio of inner to total power (Fig. 4) denoted hereafter as cone fraction (CF) is used to correct more finely for time-varying hohlraum wall albedo and residual spot motion affecting instantaneous, P_2 and P_4. Of note, Fig. 4 shows the requested CF decreasing at 6 ns to compensate for the onset of the 44.5° quads (pointed closer

to inner beam locations) at that time. Subsequently, the CF rises after that to compensate for the outer beam spots moving closer to the poles. With all these tactics in place, P_2 and P_4 drive asymmetry can in principle be zeroed out for all time.

It is instructive to estimate the sign and magnitude of the residual picket P_4 drive asymmetry in the absence of outer beam temporal phasing. The outer beam pointing is constrained to be fixed to keep the peak P_4 drive asymmetry close to zero. We use an analytic viewfactor[45] that includes the geometric smoothing S_n for mode n. Each cone contributes an amount equal to $(2n+1)P_n(\theta)S_n\epsilon/(F+1)$ to the total picket $\frac{P_n}{P_o}$ drive flux. $P_n(\theta)$ is the magnitude of the Legendre polynomial P_n evaluated at the respective cone spot centroid angle θ and ϵ is the fraction of the cone energy to the total energy (here we are interested in the picket of the laser pulse) inversely weighted by the square of the distance between the cone spots and the capsule center. F is the ratio of recirculating to laser produced x-ray flux = $\alpha_w/[(1-\alpha_w)+(A_{LEH}+A_{caps})/A_{hohl}]$, that depends both on the wall albedo (α_w) and the relative areas of the LEH (A_{LEH}) and the capsule (A_{caps}) to the hohlraum wall area (A_{hohl}) (= 0.17 in this case). Because the wall albedo α_w is small during the laser picket that launches the first shock (≈ 0.5 for fixed power $(1-\alpha_w) = 0.45/(T_{r0}^{0.7}\ t^{0.4})$ where T_{r0} is defined at 1 ns after the start of picket ≈ 1.1 heV)[46], F is also small, ≈ 0.7, hence any laser driven asymmetries get magnified. Without outer beam phasing, the centroid of the outer beams is 4° closer (polar angle of the beam spot θ ≈ 50° vs 46°) to the inner spots (θ ≈ 85°). Hence, to keep P_2 near zero, one would have to further reduce the picket CF from 0.2 in Fig. 4 to ≈ 0.1 per equation above. That in turn would accentuate the fraction of drive at ≈ θ = 45° where the outer beam spots are located, hence driving the resultant P_4/P_0 at the capsule more negative, by ≈ -7%. In essence, the picket drive would approximate a single cone per side geometry such as for prior Nova hohlraums that exhibit a_4 asymmetry[25]. This undesirable change in P_4 is further magnified by two other effects: when including the 44.5° beams, the closer proximity of the outer beam centroid to the capsule has both increased its weighted ϵ by 5% (and reduced the inner cone ϵ by 10%) and reduced its P_4 smoothing factor by 33% (S_4 going from 0.03 to 0.045). Such a -7% excursion in picket P_4 from near zero would lead (per simulations) to a significant P_4 <ρr> mode in the stagnated fuel uniformity, impacting performance[4, 5].

B. Experimental Parameters

Figure 5 summarizes the target and laser utilized on this experimental series. To compare efficiency to prior 0.96 mg/cc high gas-fill CH 4-shock adiabat designs[42, 47], we used the same 5.75 mm diameter hohlraum, albeit Au versus the more efficient Au-lined DU. We chose a 2x lower hohlraum gas-fill ρ_{He} of 0.45 mg/cc to avoid significant backscatter[21], thus reducing the energy stored in the hohlraum gas, yet allow for a moderate level of gas tamping of the hohlraum wall blow-off[28]. The specific dimensions of the hohlraum and laser pointing are set using the radiation hydrodynamics code Hydra[48]. To mitigate potential late time absorption of outer cone in the high-Z plasma ablated off the endcaps laser entrance holes (LEHs) that could make the effectiveness of the other tactics ambiguous, we used a larger LEH diameter (3.64 versus usual 3.37 or 3.1 mm initial diameter). Just outside the 50 µm thick Au annuli that form the LEHs are 150 µm thick 4.05 mm inner diameter Al rings for overlaying the sub-µm CH foils that seal the

hohlraum gas. Since these Al rings are ~200 µm larger in radius than the Au annuli, their edges are recessed and will only have a limited view of the inside of the hohlraum, so we expect that the x-ray driven Al blow-off is limited providing at best a mild perturbation to the LEH plasma conditions. Nevertheless, the level of CBET at peak power could have been altered based on simulations[49] of the more extreme condition of the Au-LEH and Al-rings having the same radius. However, we expect any effects to be systematic since the current experimental series did not change sensitive parameters to the Al plasma evolution such as gas-fill, peak power or laser pointing. The simulations used to design this series did not account for the Al ring. The hohlraum length was changed from 9.45 used on prior experiments to 10.1 mm based on optimization of the outer beam pointing and hence LEH clearance to reduce the early time low mode P_4 drive asymmetry. The 50° cone beams are aimed at z = ±2.8 mm, while the delayed 44.5° cone beams are aimed at z = ±2.1 mm. Such a separation of 0.7 mm is ~ 2x larger than usually used, providing more angular leverage to compensate for spot motion.

As shown in Fig. 5b, we use a 10% smaller inside radius and 20% thinner ablator than the original CH 4-shock design[42], identical to the smaller capsule[29] used for the CH 3-Shock design in a 0.6 mg/cc fill 6.72 mm diameter hohlraum[50]. This capsule size reduction, as discussed in a prior section, is a first step in improving propagation of the inner cone beams in the hohlraum by requiring a 20% shorter pulse, 14.1 ns versus the prior 17.5 ns long drive pulse[47]. Fig. 5b shows that the thickness of the capsule ablator to be 170 µm, with the usual buried Si-doped preheat shielding layers, and a 16 µm inner undoped CH layer that mimics the mass of 62 µm of DT ice in the layered design.

Fig. 5c compares the pulse shape designed for this experiment (solid line) with the pulse shape (dashed line) for a typical 3 shock HDC design at 0.3 mg/cc gas-fill in the same size hohlraum[22, 51]. Of note is the much longer and weaker trough (1 TW level in inset) and over 2x longer pulse duration. The total energy on Fig. 5c is 1.1 MJ, also substantially less than the 1.7 MJ 0.96 mg/cc fill CH 4-shock design[47] reflecting expectations of improved coupling efficiency in the lower gas-fill. For the same reason, the peak power is also much lower (280 versus 360 TW), which also allows for more flexibility in setting the ratio of inner to total peak power away from the natural 1/3 ratio. Indeed, Fig. 4 shows that the requested inner to total cone fraction during peak power was 0.44, to deliver more energy to the hohlraum waist late in time.

Summarizing, the primary comparison goal is to demonstrate a symmetric implosion at 2 and 1.3x longer pulse length than had been previously accomplished in a low gas-fill hohlraum of the same size (the 3-shock HDC design) and with the same size capsule in a less efficient 17% larger radius hohlraum (the 3-shock CH high-foot design), respectively. A secondary goal is to show considerably higher coupling efficiency than the prior high gas-fill CH 4-shock adiabat-shaped design using the same diameter hohlraum. The ultimate goal is to use such a subscale demonstration as the basis for scaling up the laser energy and power, and the hohlraum and capsule sizes to drive a robust low-adiabat implosion utilizing the full capabilities of the NIF laser system, as discussed further in Section IV.

Commented [IN1]: Which one is this 1.3x longer campaign?

Commented [LL2R1]: The CH, why says respectively at end.

C. Measurement Techniques

To check capsule performance, we used 3 different experimental platforms[52] denoted as “KeyHole”, “SymCap”, and “2DConA” illustrated in Fig. 6.

First, the KeyHole platform utilizes a D_2 liquid filled capsule with a re-entrant cone on one side to allow for streaked optical velocimetry[53] measuring the leading shock velocity, and breakout and merge timings from inside of the shell[54-56]. We employed a 3-axis line-imaging velocimetry (polar angles θ = 0°, 45°, and 90°) to evaluate the P_2 and P_4 symmetry of the shocks[57]. The picket power and timing of the different steps of the laser pulse up to peak power are then adjusted, if needed, to ensure that the desired shock speeds and merge depths are close to optimal (i.e., to the prior high gas-fill shots) thus ensuring a low in-flight fuel adiabat.

Second, we checked the symmetry of the imploded capsule using CH capsules with no DT fuel layer denoted "SymCap". The symmetry of the drive is tested from the Legendre mode decomposition of the 17% contour line of the multi-keV x-ray self-emission images of the imploded core taken with 100 ps temporal and 11 µm spatial resolution[58] over the duration of the x-ray self-emission (≈ 200 ps). The surrogate capsule which has the same outer radius and initial areal density as the designed DT shot target is ablatively accelerated and integrates time dependent drive asymmetry in the manner identical to that of the DT layered shell. The shape of the SymCap self-emission core image provides information on the integrated drive asymmetry through the duration of the X-ray drive.

Third, we infer the in-flight symmetry of the drive using 100 ps, 60 µm resolution 2D x-ray backlit imaging[59] of the imploding capsule using the target denoted as "2DConA". The 2DConA backlit image provides both the radius vs time (hence peak implosion velocity) and distortion of the shell in flight during the observation window (typically covering 600 ps, beginning ~1 ns before peak stagnation time (bang time)). An Fe back-lighter with a He-α transition line at 6.7 keV was chosen to provide good contrast (between 1 and 2 optical depths at the shell limb).

We also use these platforms to make simultaneous x-ray and optical measurements of the hohlraum bubble dynamics[60] and the laser to hohlraum coupling[61, 62]. The time evolution and azimuthal shape of the outer bubble is captured by a 100 ps, 80 µm resolution gated self-emission imaging system situated at the north pole of the hohlraum. Additionally, we image the x-ray emission escaping through the wall as seen from an equatorial view. Since the nominal 30 µm thickness of the hohlraum wall is opaque to the 10 keV Au L-shell radiation, we utilized "thin-wall patches" to monitor the transport of the inner cone beam power to the waist of the hohlraum[63]. The thickness of Au on the thin-wall patches is set nominally to 8 µm, greater than the expected x-ray Marshak wave depth[7, 34] so as not to affect the local hohlraum albedo[64] and hence drive symmetry, but thin enough to transmit Au L shell radiation. During peak power, we can then image with 220 µm resolution accuracy the multi-keV x-rays transmitted through the thin-wall section as a measure of the location where the inner beams deposit their energy. As the inner cone beam transport is interrupted by the outer gold plasma bubbles before reaching their projected destination, we can directly observe the reduction or absence of the x-ray emission. We also infer the peak radiation drive temperature through the bottom LEH at a polar angle of 143°, using the multichannel soft x-ray power diagnostic Dante[65] corrected for LEH closure and subtracting out the annulus of emission outside the LEH[66], and finally, a measurement of the level of laser backscatter on a few representative beams is also performed

III. Results

A. **Shock Symmetry**

To ensure a low in-flight adiabat of the implosion, the velocity and merge times of the different shocks need to be controlled[16] to within 5% and ± 100 ps respectively. The requested laser powers are well within the capabilities of the NIF system, so adjustments to the power levels of the different laser epochs after the experiment presented no difficulties. Of greater interest was the polar angle uniformity of the shock timing / velocity, assessed using the 3-axis KeyHole target described above. Ensuring shock symmetry by proper choice of inner beam cone fraction (CF) and pointing is particularly important for the thicker ablator CH versus HDC designs. This is because any low mode ($l < 5$) first shock asymmetry travels further so can seed more non-radial ablator motion leading to significant fuel areal density non-uniformities[67, 68] at stagnation time that can thwart ignition even for round cores. To mitigate the P_2 drive asymmetry throughout the pulse, the cone fraction is readjusted every ≈2 ns increments to compensate for time-varying albedo as the laser rises to launch further shocks[69] and for any residual spot motion[7] not correctable by the one-time temporal beam phasing. To clearly measure the timing and velocity of the individual shock fronts separately, the laser pulse is adjusted by having a wider separation between the different epochs (shown in Fig. 9) as compared with the laser used in the following implosion experiments.

The streaked data from shot N210928 obtained with VISAR on Figure 7a shows successively the breakout of the 1st shock from the CH, then the merges of shocks 1 and 2, and just for the equator channel only, the merger of shocks 2 and 3 and shocks 3 and 4 (as indicated in the figure) in the liquid deuterium. The measure of the first breakout time at the 3 different angular positions around the capsule shows good uniformity as does the first shock velocity and the merger timing of shocks 1 and 2.

Figure 7b shows that the equatorial shock velocities (filled bars) match within a few % the ones intended to be replicated (open bars) for all 4 shocks. The open bars correspond to the measure velocities from the comparison shot N140912, an adiabat-shaped 4-shock CH target in a high gas-fill (0.96 mg/cc) hohlraum having the same dimensions but using a slightly smaller (3.37 mm) LEH and a 12% larger and 25% thicker capsule. Hence, the drive levels for the following "SymCap" shots were only slightly adjusted based on the results of these KeyHole shots using simulated sensitivity curves. For the ensuing implosion shots, the 2nd, 3rd, and 4th shock launch times were moved by +0.2, -0.9 and -1.4 ns respectively to provide an optimum shock timing where merges occur just beyond the DT fuel/gas interface.

Figure 7c shows the Legendre modal decomposition of the shock break-out and the 1-2 merge timings. The P_2 and P_4 shock timings were controlled to better than 50 and 75 ps, respectively. It should be noted that this KeyHole also used azimuthal beam phasing, thus the first shock is launched using just the inner and 50a beams on, while the second shock is launched after 6 ns (see Fig. 3d) with all beams on. The good synchronization exhibited on both break-out and merge of the first 2 shocks is a first indication of the beneficial impact of temporal beam staggering.

Since only half of the 50° outer quads were present during the picket, a question that remains is how their azimuthal clocking may have biased the inferred first shock strength measured at the equatorial and 45° VISAR lines of sight. A simple viewfactor calculation shows that we expect < 15 ps in the first shock break-

out time and in the shock 1-2 merger time relative to the non-azimuthally beam phased case. The variation is small because of the strong (> 20x) geometric smoothing[30] of the mode 4 outer beam illumination pattern at the capsule for an outer spot stand-off distance to capsule radius ratio of 4. Another consequence of azimuthal beam phasing is that we would expect worse imprinting of perturbations on the capsule by the x-ray shadows[70] of the fill-tube not yet vaporized during the picket from any given 50° quad due to its 2x increase in power over the non-azimuthally phased case. For the non-azimuthally phased case, the 50° quad split beams form a single ring as stated previously, so that we expect no worse shadow seeding than the usual case of adjoining 45° and 50° beams when both cones are on during the picket drive. The choice of using the adiabat-shaped drive here should mitigate the ablation front growth of these perturbations.

B. Radial Wall Dynamics

The transport of inner cone beams in a low initial gas-fill density hohlraum is affected by beam obscuration from the coronal plasma ablated at the outer cone spot (bubble plasma). According to hydrodynamic simulations, the tip of the bubble has the maximum radial excursion at z = +/- 3 mm, close to the initial location where the 50° outer beam impinges onto the hohlraum wall. In this plane, the inner cone beam power has an imprint around the hohlraum axis corresponding to a radius smaller than 1.8 mm. So, if the inner radius of the bubble ring tips seen from the top of the hohlraum through the LEH become smaller than 1.8 mm, the low-density Au bubble intersects the inner cone beam path and starts absorbing some of the inner cone beam power before it can reach the waist of the cylindrical hohlraum.

Figures 8a and b compare the images obtained through the LEH using an x-ray framing camera on the hohlraum axis for two shots not using (N211129) and employing (N211229) the azimuthal beam phasing technique described earlier. The round outer edge of the emission is the edge of the LEH corresponding to the 1.82 mm initial radius. So, the bright emission seen on this view can be understood as the Au bubble plasma already entering the inner cone beam path. The time interval of each frame is set to 500 ps. It should be noted that the outer cone quads hitting the cylindrical part of the hohlraum have slightly different clocking on the top and bottom sides of the hohlraum. The 4 quads on the top and bottom sides are clocked ±5.63° with respect to each other. Therefore, the partial overlap of top and bottom rings of beams makes the bubbles (troughs) appear broader (narrower) than they actually are. Figures 8c and d show the radial intensity profile of the image through a bubble tip without and with azimuthal beam phasing. One can see that the bubble tips have progressed further in the azimuthal beam phased case. Moreover, the bubble tip shows rapid slow down attributed to back pressure from the plasma stagnation on the hohlraum axis. The profiles also showed brightening of the spike tip after 13.4 ns. This suggests a buildup of the bubble tip density due to stagnation of the tip, which could also lead to further absorption of, and heating by, the inner cone beam power. The densification could be augmented by Rayleigh-Taylor hydro-instability growth that saturates later in 3D vs 2D geometry[71], which was not accounted for in the earlier discussion on the potential benefits of ABP.

Figure 9a overlays the trajectories of the bubble tip r_{bub}, defined as the maximum gradient point of the radial profile, with the laser pulse shapes. The black and red circles are from the SymCap shot N211129 and KeyHole shot N211003, respectively, both without azimuthal beam phasing. The gray band denotes

the inner beam extent at the bubble tip plane, showing partial interception of inner beams by peak power. It is also already clear from this plot that the bubble trajectories are not ballistic, that is, do not extrapolate to the beginning of the outer cone laser pulse. Specifically, the delay in the bubble growth measured during the KeyHole shot can be attributed to the 1.4 ns delay in the leading edge of the main drive designed to provide wider temporal separation of the shock mergers for better visibility on the VISAR streak camera data. Therefore, by advancing the r_{bub} data obtained on the KeyHole shots by 1.4 ns, it is possible to stitch up the two data sets and obtain a continuous bubble growth history from the early phase (equivalent to 11.0 ~12.6 ns) to the late phase (12.7 ~ 14.2 ns). Figure 9b shows the bubble tip trajectory obtained as a result of this process from the KeyHole and SymCap experiments. The closed circles are from shots N211003 and N211229 without azimuthal beam phasing, while the open circles represent the bubble tips and troughs from the two shots N210928 and N211229 with azimuthal beam phasing. Note that the bubble tips are gradually slowing down, attributable to the increase of gas-fill back-pressure in this convergent geometry.

By extrapolating back as if the bubble trajectory were ballistically launched (dashed line in Fig. 9b) at a fixed 300 μm/ns maximum bubble speed $v_{bub,}$ the bubble would appear to have emerged from the hohlraum wall after a significant delay of 7 ns. This is significantly different from what was observed on the 3 shock HDC design[28]. In the case of the 3 shock HDC design (which has a strong picket and trough pulse, see Fig. 5c), the extrapolation of the bubble tip trajectory indicated that the motion of the Au-He boundary is triggered by the outer picket pulse of energy E. However, for this 4 shock CH design, the measured trajectory indicates that the bubble growth initiated by the picket of the laser pulse stagnates during the trough and is then effectively relaunched during the second epoch of the pulse at t ~ 6 ns. It is instructive to quantify the expected bubble speed just after the picket is delivered. Scaling from the 3-shock HDC shot N171010 in Fig. 5c with v_{bub} = 375 μm/ns [28] and using the scaling $(E/\rho_{He})^{0.2}$, we would expect the 4-shock picket $v_{bub} \approx 290$ μm/ns for E being 2.5x smaller and ρ_{He} 1.5x larger. Hence, if the bubble motion were to be ballistic, it would have reached the hohlraum axis by ≈ 10 ns, in clear disagreement with the measured data. When azimuthal beam phasing (ABP) is employed, the growth of the spike region is advanced by 300 μm and the trough region is behind by 500 μm as seen in Fig. 9b. Therefore, while ABP altered the growth pattern of the bubble plasma, its benefit to the inner cone power transport ($\Delta r_{bub} \approx$ +100 μm on average) appears modest. We will discuss more about how ABP affected the inner cone transport in the next section.

C. Inner Cone Propagation

When the Au plasma ablated off the waist portion of the hohlraum wall collides with the ablated CH plasma from the shell, a ridge of higher density is created at a radius typically 2.1 mm for a 2.88 mm radius hohlraum[28], as shown in Fig. 1. During the main drive of the pulse, the inner cone beam power transmitted through the outer bubbles is stopped by this density ridge creating the x-ray emission seen through the thin-wall patches on the equator of the target.

Figure 10a shows the target design with the results of ray tracing. Four different cone spots are shown in different color (23.5° in red, 30° blue, 44.5° green, 50° orange). The rays of inner cone beams are terminated at the cylindrical surface of the density ridge located at a radius of 2.1 mm. Due to the different

inner beam clocking of NIF beams on the top and bottom halves of the hohlraum of 22.5° in azimuth, the patterns that include near and far beam emission are different between the two halves of the hohlraum. We focus on the top beams shown in Figs. 10b and c for which the azimuthal view is along the vertical, and for which the near and far 23.5° strongly overlap, as do the 30° beams. Figure 10b shows the data for the shot without ABP, indicating that the bubble growth has little azimuthal modulation, with an 8-fold pattern in phase with the 50° beams. Figure 10c shows the data for the shot employing ABP. It displays that the 8-fold pattern has become a 4-fold pattern in-phase with the 50° beams turned on early. Those 50° bubble tips (troughs) are more in phase (within 5.6°) with the 23.5° (30°) beams, and the same is true for the bottom beams. Therefore, with ABP, we expect the 23.5° beams to experience more clipping by the bubble compared to the 30° beams.

The imaging data from the equator is shown in Fig. 10d and e without (N211129) and with ABP (N211229). Metrology of the thin-wall part showed that the actual wall thickness ranged from 6 to 10 µm between shots and top and bottom halves. For better visibility of the structure, the thickness variability, and the location dependent x-ray absorption due to varying chord length was compensated for, though residual variations in overall brightness could point to uncertainties in metrology and photon spectrum assumed. Nonetheless, well outside those uncertainties, a comparison of Figure 10d and e show the reduction in the time-integrated x-ray brightness of the 23.5° beam seen almost head-on that can be attributed to the greater 50° bubble growth with ABP. Conversely, the two 30° quads appear brighter in Fig 10e, a likely consequence of better power transport to the midplane since these quads propagate between the bubbles in the ABP shot.

D. Core Symmetry

The drive symmetry integrated throughout the drive pulse is evaluated by analyzing the distortion of the self-emission x-ray image of the imploded core. Figure 11 shows the self-emission images and amplitude of the Legendre modes of the 17% contour line of the core self-emission. In the absence of additional symmetry tuning using CBET ($\Delta\lambda$ = 0 Å), shot N211229 with ABP showed significantly more oblate core shape (a_2 = -28 ± 3 µm) than shot N211129 without ABP (a_2 = -17 ± 3 µm). This indicates that ABP had an adverse effect on drive symmetry control that can be attributed to more absorption of the 23.5° cone beams at the bubble tips over-compensating for the diminished absorption at the troughs of the 30° cone beams as shown in Fig. 10. Additionally, the a_4 component (shown by squares in Fig. 11) with ABP was also much larger, which we attribute partially to mode coupling since a_2/a_0 was significantly large (-66%). Given the limited number of shots and that the advantages of ABP on providing a large positive P2 drive correction had not materialized, we decided to pursue adding wavelength separation (wavelength shift of inner cone beams relative to outer cone beams) without ABP, to reach time-integrated symmetry close to round before showing relevant time-resolved symmetry control using radiography. Introducing CBET is expected to predominantly affect the peak power asymmetry, however, simulations predicted a small effect on the picket asymmetry as well. We hence also compensated for CBET in the picket[68] by decreasing its CF by -0.02 (-10%) per 1 Å $\Delta\lambda$. As seen on Fig. 11, the a_2 core asymmetry of subsequent shots not employing ABP showed a positive correlation to wavelength separation tuning ($\Delta a_2/\Delta\lambda$ = 14 µm/Å). This sensitivity is 1.5-2x less than observed for other implosions in low gas-fill hohlraums[72, 73], and is attributed

to the 30-40% lower peak power and hence laser peak intensity (recall CBET transfer fraction ~ I). Fig 11 shows that only 2 additional experiments (shots N220222 and N220301) were needed to zero-out a_2 and kept a_4 nearly zero within error bars.

Figure 12 shows the time integrated x-ray emission image observed through the thin-wall patch for $\Delta\lambda$ = 0 (N211119) and 1 Å (N220222). When we do not use wavelength separation, the x-ray signal from the 23.5° and 30° cone spots are almost comparable. However, when the wavelength of inner cone beams is 1 Å longer than the outer cone beams, the intensity of the 30° cone beam spot becomes 4x brighter while the 23.5° cone spot remains at a similar intensity. This suggests that transfer between outer and inner beams is preferentially involving the 30° rather than 23.5° cone. So, one can conjecture that $da_2/\Delta\lambda$ could increase faster with ABP since it is the transmitted 30° beams that is preferentially boosted by $\Delta\lambda$. However, the disadvantage would be an increase in the azimuthal mode 4 at the equator as most of the inner cone peak power would be delivered by the 30° beams. It is also doubtful that applying an available wavelength separation[74, 75] between 23.5° and 30° to transfer back to 23.5° could ameliorate the situation given Fig. 10e showing the 50° bubbles greatly reduce the 23.5° beam signal. By contrast, this strategy could eventually be used to transfer energy between 23.5 and 30° cones for the non-ABP case if warranted. However, for this series we chose to set the polar x-ray imager to a low magnification to observe bubble dynamics, rather than to perform high magnification imaging required to accurately observe any core azimuthal mode 4 asymmetry that may need fixing. This measurement would be taken up in a follow-up campaign.

Figure 13 shows that the progressively improved core P_2 asymmetry from the successive shots, using ABP and then adding $\Delta\lambda$ without ABP as shown in Fig. 11, correlates well with the measured increase in the x-ray emissivity averaged over the thin-wall sections. This is consistent with more inner beam power reaching the equatorial drive regions providing a more prolate drive.

E. Hohlraum Energetics

The inferred peak radiation temperature at the capsule was 287 ± 4 eV on shot N211129. The radiation temperature measured at the same relative time (2.8 ns) after the start of peak power to account for increasing albedo over time was 294 ± 4 eV for the high gas-fill (0.96 mg/cc) implosion shot N210411 [47]. The higher gas-fill shot N210411 used 360 vs 280 TW peak power, a 15% larger capsule in a shorter (9.45 vs 10.1 mm) same radius hohlraum, having a smaller LEH (3.1 mm vs 3.64 mm) and Au-lined DU versus Au wall. Accounting for the 10% difference in peak x-ray drive and correcting for the hohlraum and capsule loss differences[76] (+4% for shorter hohlraum, +5% for smaller LEH, -4% for larger capsule losses, +7% for higher albedo of Au-lined DU vs Au)[77], the low gas-fill hohlraum is demonstrating 30% more peak power efficiency. Since only ≈ 2-3% can be accounted for by having to heat 2x less the He gas-fill to multi-keV temperatures, we now consider relative backscatter losses.

Figure 14 plots the energy of backscattered laser light (for the measured 30° and 50° cones) for increasing $\Delta\lambda$ between shots N211129, N220222 and N220301. As expected, the sum of stimulated Brillouin scattering (SBS) and stimulated Raman scattering (SRS) are at a low level (3% of total laser energy) due to the initial density of the ^{4}He gas-fill in the hohlraum being below[21] 0.6 mg/cc. This is to be compared with

high gas-fill shot N171122 (2DConA equivalent of shot N210411) showing 9% backscatter losses (5x more in absolute energy), predominantly and equally divided between outer SBS and inner SRS. That still leaves 15% losses unaccounted for to explain the 30% increase in efficiency, consistent with prior comparisons to modelling[50, 78, 79].

The small observed SBS and SRS of the 30° beams do increase with wavelength separation, attributed to its laser intensity increasing as cross-beam energy transfer (CBET) to the 50° cone beams is reduced and then eventually reversed[20]. The same argument explains why the SBS of the 50° beams (solid circle) decreases as function of wavelength separation. It is instructive to compare the change in SBS to inferable change in beam power after CBET. Per simulations[24] for a change in core a_2 of +20 μm shown on Fig. 11 between $\Delta\lambda$ = 0 and 1.5 Å, the expected change in inner peak power fraction CF is +.08, or 18% of the nominal $\Delta\lambda$ = 0 Å CF = 0.44. If most of that change is attributed to the 30° beams, that is a 36% increase in 30° peak power, to be compared to the 5.2x increase in 30° SBS, consistent with being in the non-linear amplification mode of SBS. Of related interest is the level of > 170 keV "hot" electrons that can penetrate the ablator and preheat the fuel in a layered implosion and raise its adiabat, particularly detrimental for the current 4-shock low adiabat design drive. At peak power, the level of > 170 keV electrons as inferred from the Bremsstrahlung created in the Au hohlraum walls and measured by the time-resolved hard x-ray spectrometer FFLEX [80] was 15-25 J. This is well below the acceptable threshold even if occurred as early as the third shock launch and well below the 950 J measured for the 0.96 mg/cc fill shot N171122. The absence of hot electron induced hard x-ray background will also allow for a simpler time-integrated Image Plate detector rather than just a gated imager to be used in Compton radiography to measure the final stagnated fuel density profile[81].

F. In-flight Energetics and Symmetry

The X-ray backlit radiography platform denoted "2DConA" was used to evaluate the low mode distortion of the shell near its maximum velocity point for shot N220301 using $\Delta\lambda$ = 1.5Å that gave near zero core a_2 and a_4.

2DConA hohlraums are driven by only 184 beams, as 2 outer quads are needed to produce the x-ray backlighter for imaging. Traditionally, those two quads come from the 50° cone beams to provide higher intensity since their spot sizes are 10% smaller than the 44.5° beams. However, in this experiment, since the outer picket and trough drive is using only 50° cone beams, we did not want to deteriorate the foot symmetry by using two 50° quads for the backlighter. Therefore, the experiment employed an adjacent 44.5° cone quad for excitation of the backlighter. To avoid clipping of the backlighter beams by the support arms of the hohlraum, the backlighter foil is located 15.5 mm from the object (instead of standard 12 mm) and only one quad could be used.

In order to mitigate the mode 1 drive asymmetry[82] that would be imposed by this missing quad, another 44.5° quad close to its diagonal location was turned off, leaving principally a small 45°-tilt spherical harmonic mode Y_2^1 in the line-of-sight. To compensate for the missing backlighter beams and avoid a global change in the axisymmetric Legendre P_2, the power of the main drive portion (10.5 - 14.1 ns) of each of the remaining 44.5° cone beams was enhanced compared to the "SymCap" shots by a factor 8/7.

Commented [MJ3]: This came out of nowhere, we were talking about N210411 (which is equivalent to n171122 but readers don't know that) Why not use N210411 instead Reading forward, I know why, so look at my edit and see if you agree,,,,

Commented [LOL4R3]: Fixed

The residual projected Δa_2 in-flight shell asymmetry from the Y_2^1 can be estimated by the analytic viewfactor from before as $\Delta a_2 \leq (r_o - a_0)\left(\frac{5S_2\varepsilon/14}{3(F+1)}\right)\frac{1}{\sqrt{2}}$, where r_0 is the initial inside radius of the capsule, a_0 is the radius at deceleration (such that $r_0 - a_0 \approx 700$ µm is the distance traveled under acceleration by the shell) and S_2 is the geometric smoothing of a mode 2. For $S_2 = 0.45$, $\varepsilon = 0.5$, an albedo $\alpha_w = 0.8$ and LEH to wall area $A_{LEH}/A_{wall} = 0.1$, hence F = 3, we arrive at a small correction $\Delta a_2 \leq +3.3$ µm.

Figure 15a shows a selection of the backlit images obtained. The spatial resolution limited by the 50 µm pinhole diameter is about 60 µm. Typical exposure duration of the gated MCP detector is 100 ps, and the estimated motion blur is about 25 µm in the radial direction. From these data, we first extract the radial profile of the image as a function of polar angle every 1° (two sets of data for left and right side of the image), then find the radius of the limb minimum transmission at each of the 360 radial lineouts, and finally obtain Legendre mode amplitudes by doing an integral transform. Given an average radiographed capsule limb circumference of 1200 µm, the number of independent measurements is 1200/60 = 20 points and the highest resolvable mode without significant correction for finite resolution is ~ 20/3 ≈ 7 . The basis of the Legendre mode decomposition (integration transform) is orthogonal but not orthonormal. Therefore, the error on the amplitude of a Legendre mode n due to noise in the contour line analysis is expected to scale as $\sqrt{2n+1}$, typically 2 µm at mode 4. Figure 15b shows the time history of the average a_0 shell limb radius (defined at minimum transmission). The peak velocity v_{imp} obtained by fitting the data set between 14.3 ns to 14.54 ns is 285 ± 15 µm/ns. It is instructive to compare the energy efficiency with the 4-shock Adiabat Shaping 2DConA shot N171122 at 0.96 mg/cc fill that used 1.67 MJ in a Au-lined DU to drive a 10% larger and 20% thicker capsule[47] that reached similar 278 µm/ns velocity. We can assume that the Au-lined DU[77] compensates for the use of a proportionately 10% thicker capsule. That leaves a 10% larger capsule that needs 10% longer pulse, so 10% more energy. So relative energy usage $1.09MJ/(1.67MJ \times 0.9) = 0.7$, so 30% better energy efficiency.

By converting the transmission of the image to optical depth, we infer a fractional mass remaining M_R/M at peak velocity of 17 ± 3%, where the uncertainty is dominated by the fraction of cold opacity assumed for the carbon (0.8 ± 0.15). This value is consistent with the indirect-drive Rocket model[7] $v_{imp} \approx 10\sqrt{T_r}\ln(M/M_R)$, where peak power T_r is in eV and v_{imp} in µm/ns.

Figure 15c shows the measured amplitude of a_2 (solid circle) and a_4 modes (open squares). Accounting for the above calculated in-flight average Δa_2 of +3 µm induced by missing drive quads, we can conclude that a SymCap implosion remains round over the crucial last 1 ns of travel within ± 2-3 µm error bars, meeting the original goals. We also note very little change in symmetry between the shell and the core at bangtime, further indication of successfully minimizing symmetry swings.

IV. Discussion

We have demonstrated time dependent P_2 and P_4 symmetry control throughout the drive in a low gas-fill, low LPI loss hohlraum at 90% capsule scale by using a low foot, temporal beam phasing, a peak CF = 0.44 and some level of CBET, while still respecting shock timing and shock strength constraints for a low adiabat

design. We believe the use of a low energy in picket and trough was the most important design choice leading to this result. This assessment is based on Fig. 9 showing a time delay in reaching final bubble growth speed, in contrast to earlier experiments using similar gas-fill but higher laser pickets and troughs that show ballistic motion of the bubble from the outset[23], thus requiring a 20% larger diameter hohlraum[50] to provide symmetry control. The temporal beam phasing, as we argued in Section IIA on analytic grounds, was essential to compensating for outer beam spot motion and large P_2 and P_4 drive symmetry swings. Simulations to be published in a future companion paper confirm this, but it would take low mix DT implosions to fully assess beam phasing importance on performance. Based on Figure 11, the inclusion of ABP affected the time integrated core P_2 in an undesirable direction, akin to adding about -1 Å of $\Delta\lambda$, as confirmed by comparisons of the x-ray images of the inner beams and bubble dynamics earlier in this paper.

The ablator v_{imp} of 285 µm/ns with 17% ablator mass remaining can be translated to the peak velocity conditions expected when adding a cryogenic DT fuel layer on the inside of the ablator. For such a layered target, we would expect a peak fuel v_{imp} ≈ 300 µm/ns with ~12% ablator mass remaining (DT replacing inner CH to conserve total mass)[83]. It means that to get to an ignition relevant[15] 360 µm/ns, i.e., 20% more v_{imp} (leaving about 5% ablator) would require 30% more peak x-ray power. 7% can be gained from using a DU-based hohlraum[77], 8% from making LEH smaller[84] (from conservative 3.64 mm to 3.37 mm), so need 15 (10)% more peak laser power (energy). The experiments presented here use a laser drive having an energy of 1.1 MJ, and 280 TW peak power, so would need 1.2 MJ, 320 TW at current scale. The important metric of time between end of laser drive and bangtime or coast time that has been shown to be key to maintaining high compression[85, 86] and high pressure[87] at bangtime would go down from 1 ns to an optimum 0.4 ns. Also, a faster implosion won't be affected by a given level of bubble growth as much, so combined with DU that has higher albedo and hence higher waist drives[77] would compensate for a smaller LEH, may only need CBET to reduce the peak CF closer to optimum 0.33. An 11% larger hydro-scaled[31, 88] design using a 6.4 mm diameter hohlraum would need 33% more energy, 22% more power, so 1.6 MJ, 390 TW. A future 2.2 MJ, 470 TW NIF capability combined with more efficient hohlraums with smaller LEH and/or a lower wall area frustrum-shaped hohlraum denoted "Frustraum"[88, 89], should allow for a further 10-20% increase in scale. Mitigating[90, 91] expected residual hydrodynamic instability growth from the support tent seed[92, 93] particular to CH designs would have to be demonstrated in parallel.

V. Summary

We have shown that a low trough which is unique to the adiabat-shaped designs when compared to other major CH designs[50, 94, 95] delays bubble growth allowing for longer CH pulses. When combined with temporal beam phasing, the issues with excessive laser spot motion leading to loss of symmetry control in low gas-fill hohlraums can also be mitigated. The low gas-fill in turn improves hohlraum efficiency by reducing backscatter and energy lost to the gas-fill. From either a hohlraum or capsule coupling perspective, the low gas-fill design has improved efficiency by a significant 30%. In short, we have extended the benefits of the low gas-fill controllable hohlraum environment to the long pulse low adiabat CH design regime. If tent instability seeding on a CH ablator can be managed or an alternate less intrusive support mechanism demonstrated[96], then this could be a worthwhile strategy for pursuing a high

compression, high gain system. Moreover, this platform could be used to study trade-offs between compression and stability, by intentionally degrading the final adiabat by shock mistiming (for example using a laser pulse having a shorter trough) or appropriately modifying the rest of the pulse. It could also be used for other higher adiabat low trough designs, such as the 3-shock version of the CH adiabat-shaped design[40] for which a 2x stronger picket but 10% shorter pulse is used, or for a Be ablator[97, 98] that by virtue of having lower melting shock pressure[99] than HDC allows in principle[16] for adiabat shaping.

In summary, excellent drive symmetry control of the main intrinsic asymmetry Legendre modes P_2 and P_4 throughout the pulse is possible for long pulse low-density filled hohlraums. This represents a 2x increase in the usable pulse length at this hohlraum scale, and an improved coupling efficiency of ~30% compared to an earlier design using higher density fill hohlraums.

ACKNOWLEDGMENTS

We thank the NIF Operations, Target Fabrication and Target Diagnostic teams. This work was performed under the auspices of the U.S. Department of Energy by Lawrence Livermore National Laboratory under Contract DE-AC52-07NA27344 and by General Atomics under contract 89233119CNA000063. The data that support the findings of this study are available from the corresponding author upon reasonable request. This document was prepared as an account of work sponsored by an agency of the United States government. Neither the United States government nor Lawrence Livermore National Security, LLC, nor any of their employees makes any warranty, expressed or implied, or assumes any legal liability or responsibility for the accuracy, completeness, or usefulness of any information, apparatus, product, or process disclosed, or represents that its use would not infringe privately owned rights. Reference herein to any specific commercial product, process, or service by trade name, trademark, manufacturer, or otherwise does not necessarily constitute or imply its endorsement, recommendation, or favoring by the United States government or Lawrence Livermore National Security, LLC. The views and opinions of authors expressed herein do not necessarily state or reflect those of the United States government or Lawrence Livermore National Security, LLC, and shall not be used for advertising or product endorsement purposes.

References

1. S. Atzeni and J. Meyer-ter-Vehn, *The Physics of Inertial Fusion*. (Oxford University Press, 2008).

2. A. L. Kritcher, R. Town, D. Bradley, D. Clark, B. Spears, O. Jones, S. Haan, P. T. Springer, J. Lindl, R. H. H. Scott, D. Callahan, M. J. Edwards and O. L. Landen, Physics of Plasmas **21** (4), 042708 (2014).

3. M. J. Edwards, P. K. K. Patel, J. D. D. Lindl, L. J. J. Atherton, S. H. H. Glenzer, S. W. W. Haan, J. D. D. Kilkenny, O. L. L. Landen, E. I. I. Moses, A. Nikroo, R. Petrasso, T. C. C. Sangster, P. T. T. Springer, S. Batha, R. Benedetti, L. Bernstein, R. Betti, D. L. L. Bleuel, T. R. R. Boehly, D. K. K. Bradley, J. A. A. Caggiano, D. A. A. Callahan, P. M. M. Celliers, C. J. J. Cerjan, K. C. C. Chen, D. S. S. Clark, G. W. W. Collins, E. L. L. Dewald, L. Divol, S. Dixit, T. Doeppner, D. H. H. Edgell, J. E. E. Fair, M. Farrell, R. J. J. Fortner, J. Frenje, M. G. G. Gatu Johnson, E. Giraldez, V. Y. Y. Glebov, G. Grim, B. A. A. Hammel, A. V. V. Hamza, D. R. R. Harding, S. P. P. Hatchett, N. Hein, H. W. W. Herrmann, D. Hicks, D. E. E. Hinkel, M. Hoppe, W. W. W. Hsing, N. Izumi, B. Jacoby, O. S. S. Jones, D. Kalantar, R. Kauffman, J. L. L. Kline, J. P. P. Knauer, J. A. A. Koch, B. J. J. Kozioziemski, G. Kyrala, K. N. N. Lafortune, S. L. L. Pape, R. J. J. Leeper, R. Lerche, T. Ma, B. J. J. Macgowan, A. J. J. Mackinnon, A. Macphee, E. R. R. Mapoles, M. M. M. Marinak, M. Mauldin, P. W. W. McKenty, M. Meezan, P. A. A. Michel, J. Milovich, J. D. D. Moody, M. Moran, D. H. H. Munro, C. L. L. Olson, K. Opachich, A. E. E. Pak, T. Parham, H.-S. S. Park, J. E. E. Ralph, S. P. P. Regan, B. Remington, H. Rinderknecht, H. F. F. Robey, M. Rosen, S. Ross, J. D. D. Salmonson, J. Sater, D. H. H. Schneider, F. H. H. Séguin, S. M. M. Sepke, D. A. A. Shaughnessy, V. A. A. Smalyuk, B. K. K. Spears, C. Stoeckl, W. Stoeffl, L. Suter, C. A. A. Thomas, R. Tommasini, R. P. P. Town, S. V. V. Weber, P. J. J. Wegner, K. Widman, M. Wilke, D. C. C. Wilson, C. B. B. Yeamans and A. Zylstra, Physics of Plasmas **20**, 070501 (2013).

4. R. P. J. Town, D. K. Bradley, A. Kritcher, O. S. Jones, J. R. Rygg, R. Tommasini, M. Barrios, L. R. Benedetti, L. F. Berzak Hopkins, P. M. Celliers, T. Döppner, E. L. Dewald, D. C. Eder, J. E. Field, S. M. Glenn, N. Izumi, S. W. Haan, S. F. Khan, J. L. Kline, G. A. Kyrala, T. Ma, J. L. Milovich, J. D. Moody, S. R. Nagel, A.

Pak, J. L. Peterson, H. F. Robey, J. S. Ross, R. H. H. Scott, B. K. Spears, M. J. Edwards, J. D. Kilkenny and O. L. Landen, Physics of Plasmas **21** (2014).

5. R. H. H. Scott, D. S. Clark, D. K. Bradley, D. A. Callahan, M. J. Edwards, S. W. Haan, O. S. Jones, B. K. Spears, M. M. Marinak, R. P. J. Town, P. A. Norreys and L. J. Suter, Phys. Rev. Lett. **110**, 075001 (2013).

6. J. Gu, Z. Dai, Z. Fan, S. Zou, W. Ye, W. Pei and S. Zhu, Phys. Plasmas **21**, 012704 (2014).

7. J. Lindl, Phys. Plasmas **2** (11), 3933-4024 (1995).

8. A. Caruso and C. Strangio, Japanese Journal of Applied Physics **30**, 1095-1101 (1991).

9. L. J. Suter, A. A. Hauer, L. V. Powers, D. B. Ress, N. Delameter, W. W. Hsing, O. L. Landen, A. R. Thiessen and R. E. Turner, Physical Review Letters **73**, 2328 (1994).

10. O. L. Landen, P. A. Amendt, L. J. Suter, R. E. Turner, S. G. Glendinning, S. W. Haan, S. M. Pollaine, B. A. Hammel, M. Tabak, M. D. Rosen and J. D. Lindl, Physics of Plasmas **6**, 2137 (1999).

11. J. D. Lindl, S. W. Haan, O. L. Landen, A. R. Christopherson and R. Betti, Physics of Plasmas **25** (12), 122704 (2018).

12. O. L. Landen, D. T. Casey, J. M. DiNicola, T. Doeppner, E. P. Hartouni, D. E. Hinkel, L. F. Berzak Hopkins, M. Hohenberger, A. L. Kritcher, S. LePape, B. J. MacGowan, S. Maclaren, K. D. Meaney, M. Millot, P. K. Patel, J. Park, L. A. Pickworth, H. F. Robey, J. S. Ross, S. T. Yang, A. B. Zylstra, K. L. Baker, D. A. Callahan, P. M. Celliers, M. J. Edwards, O. A. Hurricane, J. D. Lindl, J. D. Moody, J. Ralph, V. A. Smalyuk, C. A. Thomas, B. M. Van Wonterghem and C. R. Weber, High Energy Density Physics **36**, 100765 (2020).

13. A. J. MacKinnon, N. B. Meezan, J. S. Ross, S. Le Pape, L. Berzak Hopkins, L. Divol, D. Ho, J. Milovich, A. Pak, J. Ralph, T. Döppner, P. K. Patel, C. Thomas, R. Tommasini, S. Haan, A. G. MacPhee, J. McNaney, J. Caggiano, R. Hatarik, R. Bionta, T. Ma, B. Spears, J. R. Rygg, L. R. Benedetti, R. P. J. Town, D. K. Bradley, E. L. Dewald, D. Fittinghoff, O. S. Jones, H. R. Robey, J. D. Moody, S. Khan, D. A. Callahan, A. Hamza, J. Biener, P. M. Celliers, D. G. Braun, D. J. Erskine, S. T. Prisbrey, R. J. Wallace, B. Kozioziemski, R. Dylla-Spears, J. Sater, G. Collins, E. Storm, W. Hsing, O. Landen, J. L. Atherton, J. D. Lindl, M. J. Edwards, J. A. Frenje, M.

Gatu-Johnson, C. K. Li, R. Petrasso, H. Rinderknecht, M. Rosenberg, F. H. Séguin, A. Zylstra, J. P. Knauer, G. Grim, N. Guler, F. Merrill, R. Olson, G. A. Kyrala, J. D. Kilkenny, A. Nikroo, K. Moreno, D. E. Hoover, C. Wild and E. Werner, Physics of Plasmas **21** (5), 056318 (2014).

14. S. J. Ali, P. M. Celliers, S. Haan, T. R. Boehly, N. Whiting, S. H. Baxamusa, H. Reynolds, M. A. Johnson, J. D. Hughes, B. Watson, H. Huang, J. Biener, K. Engelhorn, V. A. Smalyuk and O. L. Landen, Physics of Plasmas **25** (9), 092708 (2018).

15. J. Lindl, O. Landen, J. Edwards and E. Moses, Phys. Plasmas **21** (2), 020501 (2014).

16. S. W. Haan, J. D. Lindl, D. A. Callahan, D. S. Clark, J. D. Salmonson, B. A. Hammel, L. J. Atherton, R. C. Cook, M. J. Edwards, S. Glenzer, A. V. Hamza, S. P. Hatchett, M. C. Herrmann, D. E. Hinkel, D. D. Ho, H. Huang, O. S. Jones, J. Kline, G. Kyrala, O. L. Landen, B. J. MacGowan, M. M. Marinak, D. D. Meyerhofer, J. L. Milovich, K. A. Moreno, E. I. Moses, D. H. Munro, A. Nikroo, R. E. Olson, K. Peterson, S. M. Pollaine, J. E. Ralph, H. F. Robey, B. K. Spears, P. T. Springer, L. J. Suter, C. A. Thomas, R. P. Town, R. Vesey, S. V. Weber, H. L. Wilkens and D. C. Wilson, Physics of Plasmas **18** (5), 051001 (2011).

17. O. A. Hurricane, D. A. Callahan, D. T. Casey, E. L. Dewald, T. R. Dittrich, T. Döppner, M. A. Barrios Garcia, D. E. Hinkel, L. F. Berzak Hopkins, P. Kervin, J. L. Kline, S. L. Pape, T. Ma, A. G. MacPhee, J. L. Milovich, J. Moody, A. E. Pak, P. K. Patel, H. S. Park, B. A. Remington, H. F. Robey, J. D. Salmonson, P. T. Springer, R. Tommasini, L. R. Benedetti, J. A. Caggiano, P. Celliers, C. Cerjan, R. Dylla-Spears, D. Edgell, M. J. Edwards, D. Fittinghoff, G. P. Grim, N. Guler, N. Izumi, J. A. Frenje, M. Gatu Johnson, S. Haan, R. Hatarik, H. Herrmann, S. Khan, J. Knauer, B. J. Kozioziemski, A. L. Kritcher, G. Kyrala, S. A. Maclaren, F. E. Merrill, P. Michel, J. Ralph, J. S. Ross, J. R. Rygg, M. B. Schneider, B. K. Spears, K. Widmann and C. B. Yeamans, Physics of Plasmas **21** (5) (2014).

18. D. T. Casey, V. A. Smalyuk, K. S. Raman, J. L. Peterson, L. Berzak Hopkins, D. A. Callahan, D. S. Clark, E. L. Dewald, T. R. Dittrich, S. W. Haan, D. E. Hinkel, D. Hoover, O. A. Hurricane, J. J. Kroll, O. L. Landen, A.

S. Moore, A. Nikroo, H.-S. Park, B. A. Remington, H. F. Robey, J. R. Rygg, J. D. Salmonson, R. Tommasini and K. Widmann, Physical Review E **90**, 011102(R) (2014).

19. A. Pak, L. Divol, A. L. L. Kritcher, T. Ma, J. E. E. Ralph, B. Bachmann, L. R. R. Benedetti, D. T. T. Casey, P. M. M. Celliers, E. L. L. Dewald, T. Döppner, J. E. E. Field, D. E. E. Fratanduono, L. F. F. Berzak Hopkins, N. Izumi, S. F. F. Khan, O. L. L. Landen, G. A. A. Kyrala, S. LePape, M. Millot, J. L. L. Milovich, A. S. S. Moore, S. R. R. Nagel, H.-S. S. Park, J. R. R. Rygg, D. K. K. Bradley, D. A. A. Callahan, D. E. E. Hinkel, W. W. W. Hsing, O. A. A. Hurricane, N. B. B. Meezan, J. D. D. Moody, P. Patel, H. F. F. Robey, M. B. B. Schneider, R. P. J. P. J. Town and M. J. J. Edwards, Physics of Plasmas **24**, 056306 (2017).

20. P. Michel, L. Divol, E. A. Williams, S. Weber, C. A. Thomas, D. A. Callahan, S. W. Haan, J. D. Salmonson, S. Dixit, D. E. Hinkel, M. J. Edwards, B. J. Macgowan, J. D. Lindl, S. H. Glenzer and L. J. Suter, Phys Rev Lett **102** (2), 025004 (2009).

21. G. N. Hall, O. S. Jones, D. J. Strozzi, J. D. Moody, D. Turnbull, J. Ralph, P. A. Michel, M. Hohenberger, A. S. Moore, O. L. Landen, L. Divol, D. K. Bradley, D. E. Hinkel, A. J. Mackinnon, R. P. J. Town, N. B. Meezan, L. Berzak Hopkins and N. Izumi, Physics of Plasmas **24** (5), 052706 (2017).

22. L. Divol, A. Pak, L. F. Berzak Hopkins, S. L. Pape, N. B. Meezan, E. L. Dewald, D. D. M. Ho, S. F. Khan, A. J. Mackinnon, J. S. Ross, D. P. Turnbull, C. Weber, P. M. Celliers, M. Millot, L. R. Benedetti, J. E. Field, N. Izumi, G. A. Kyrala, T. Ma, S. R. Nagel, J. R. Rygg, D. Edgell, A. G. Macphee, C. Goyon, M. Hohenberger, B. J. MacGowan, P. Michel, D. Strozzi, W. S. Cassata, D. Casey, D. N. Fittinghoff, N. Gharibyan, R. Hatarik, D. Sayre, P. Volegov, C. Yeamans, B. Bachmann, T. Döppner, J. Biener, J. Crippen, C. Choate, H. Huang, C. Kong, A. Nikroo, N. G. Rice, M. Stadermann, S. D. Bhandarkar, S. Haan, B. Kozioziemski, W. W. Hsing, O. L. Landen, J. D. Moody, R. P. J. Town, D. A. Callahan, O. A. Hurricane and M. J. Edwards, Physics of Plasmas **24** (5), 056309 (2017).

23. J. E. Ralph, O. Landen, L. Divol, A. Pak, T. Ma, D. A. Callahan, A. L. Kritcher, T. Döppner, D. E. Hinkel, C. Jarrott, J. D. Moody, B. B. Pollock, O. Hurricane and M. J. Edwards, Physics of Plasmas **25** (8), 082701 (2018).

24. D. A. Callahan, O. A. Hurricane, J. E. Ralph, C. A. Thomas, K. L. Baker, L. R. Benedetti, L. F. Berzak Hopkins, D. T. Casey, T. Chapman, C. E. Czajka, E. L. Dewald, L. Divol, T. Döppner, D. E. Hinkel, M. Hohenberger, L. C. Jarrott, S. F. Khan, A. L. Kritcher, O. L. Landen, S. LePape, S. A. MacLaren, L. P. Masse, N. B. Meezan, A. E. Pak, J. D. Salmonson, D. T. Woods, N. Izumi, T. Ma, D. A. Mariscal, S. R. Nagel, J. L. Kline, G. A. Kyrala, E. N. Loomis, S. A. Yi, A. B. Zylstra and S. H. Batha, Physics of Plasmas **25** (5), 056305 (2018).

25. S. G. Glendinning, P. Amendt, B. D. Cline, R. B. Ehrlich, B. A. Hammel, D. H. Kalantar, O. L. Landen, R. E. Turner, R. J. Wallace, T. J. Weiland, N. Dague, J. P. Jadaud, D. K. Bradley, G. Pien and S. Morse, Review of Scientific Instruments **70** (1), 536-542 (1999).

26. R. E. Turner, P. Amendt, O. L. Landen, S. G. Glendinning, P. Bell, C. Decker, B. A. Hammel, D. Kalantar, D. Lee, R. Wallace, D. Bradley, M. Cable, R. S. Craxton, R. Kremens, W. Seka, J. Schnittman, K. Thorp, T. J. Murphy, N. Delamater, C. W. Barnes, A. Hauer, G. Magelssen and J. Wallace, Physics of Plasmas **7** (1), 333-337 (2000).

27. M. L. Spaeth, K. R. Manes, D. H. Kalantar, P. E. Miller, J. E. Heebner, E. S. Bliss, D. R. Spec, T. G. Parham, P. K. Whitman, P. J. Wegner, P. A. Baisden, J. A. Menapace, M. W. Bowers, S. J. Cohen, T. I. Suratwala, J. M. Di Nicola, M. A. Newton, J. J. Adams, J. B. Trenholme, R. G. Finucane, R. E. Bonanno, D. C. Rardin, P. A. Arnold, S. N. Dixit, G. V. Erbert, A. C. Erlandson, J. E. Fair, E. Feigenbaum, W. H. Gourdin, R. A. Hawley, J. Honig, R. K. House, K. S. Jancaitis, K. N. LaFortune, D. W. Larson, B. J. Le Galloudec, J. D. Lindl, B. J. MacGowan, C. D. Marshall, K. P. McCandless, R. W. McCracken, R. C. Montesanti, E. I. Moses, M. C. Nostrand, J. A. Pryatel, V. S. Roberts, S. B. Rodriguez, A. W. Rowe, R. A. Sacks, J. T. Salmon, M. J. Shaw, S. Sommer, C. J. Stolz, G. L. Tietbohl, C. C. Widmayer and R. Zacharias, Fusion Science and Technology **69** (1), 25-145 (2017).

28. N. Izumi, D. T. Woods, N. B. Meezan, J. D. Moody, O. L. Landen, L. Divol, H. Chen, D. A. Callahan, M. Hohenberger, A. L. Kritcher, D. T. Casey, M. D. Rosen, J. S. Ross, M. B. Schneider, M. J. Edwards and W. W. Hsing, Physics of Plasmas **28** (2), 022706 (2021).

29. T. Döppner, D. E. Hinkel, L. C. Jarrott, L. Masse, J. E. Ralph, L. R. Benedetti, B. Bachmann, P. M. Celliers, D. T. Casey, L. Divol, J. E. Field, C. Goyon, R. Hatarik, M. Hohenberger, N. Izumi, S. F. Khan, A. L. Kritcher, T. Ma, B. J. MacGowan, M. Millot, J. Milovich, S. Nagel, A. Pak, J. Park, P. Patel, R. Tommasini, P. Volegov, C. Weber, O. L. Landen, D. A. Callahan, O. A. Hurricane and M. J. Edwards, Physics of Plasmas **27** (4), 042701 (2020).

30. S. M. Pollaine, Nuclear Fusion **40**, 2061-2069 (2000).

31. R. Nora, R. Betti, K. S. Anderson, A. Shvydky, A. Bose, K. M. Woo, A. R. Christopherson, J. A. Marozas, T. J. B. Collins, P. B. Radha, S. X. Hu, R. Epstein, F. J. Marshall, R. L. McCrory, T. C. Sangster and D. D. Meyerhofer, Physics of Plasmas **21** (5), 056316 (2014).

32. M. J. Edwards, J. D. Lindl, B. K. Spears, S. V. Weber, L. J. Atherton, D. L. Bleuel, D. K. Bradley, D. A. Callahan, C. J. Cerjan, D. Clark, G. W. Collins, J. E. Fair, R. J. Fortner, S. H. Glenzer, S. W. Haan, B. A. Hammel, A. V. Hamza, S. P. Hatchett, N. Izumi, B. Jacoby, O. S. Jones, J. A. Koch, B. J. Kozioziemski, O. L. Landen, R. Lerche, B. J. MacGowan, A. J. MacKinnon, E. R. Mapoles, M. M. Marinak, M. Moran, E. I. Moses, D. H. Munro, D. H. Schneider, S. M. Sepke, D. A. Shaughnessy, P. T. Springer, R. Tommasini, L. Bernstein, W. Stoeffl, R. Betti, T. R. Boehly, T. C. Sangster, V. Y. Glebov, P. W. McKenty, S. P. Regan, D. H. Edgell, J. P. Knauer, C. Stoeckl, D. R. Harding, S. Batha, G. Grim, H. W. Herrmann, G. Kyrala, M. Wilke, D. C. Wilson, J. Frenje, R. Petrasso, K. Moreno, H. Huang, K. C. Chen, E. Giraldez, J. D. Kilkenny, M. Mauldin, N. Hein, M. Hoppe, A. Nikroo and R. J. Leeper, Physics of Plasmas **18** (5), 051003 (2011).

33. B. Scheiner and M. Schmitt, Physics of Plasmas **26** (2), 024502 (2019).

34. M. D. Rosen, Physics of Plasmas **3** (5), 1803-1812 (1996).

35. V. N. Goncharov, J. P. Knauer, P. W. McKenty, P. B. Radha, T. C. Sangster, S. Skupsky, R. Betti, R. L. McCrory and D. D. Meyerhofer, Phys. Plasmas **10**, 1906-1918 (2003).

36. J. L. Peterson, L. F. Berzak Hopkins, O. S. Jones and D. S. Clark, Phys. Rev. E **91**, 31101 (2015).

37. D. S. Clark, J. L. Milovich, D. E. Hinkel, J. D. Salmonson, J. L. Peterson, L. F. Berzak Hopkins, D. C. Eder, S. W. Haan, O. S. Jones, M. M. Marinak, H. F. Robey, V. A. Smalyuk and C. R. Weber, Physics of Plasmas **21** (11), 112705 (2014).

38. J. L. Milovich, H. F. Robey, D. S. Clark, K. L. Baker, D. T. Casey, C. Cerjan, J. Field, A. G. MacPhee, A. Pak, P. K. Patel, J. L. Peterson, V. A. Smalyuk and C. R. Weber, Physics of Plasmas **22** (12), 122702 (2015).

39. K. L. Baker, H. F. Robey, J. L. Milovich, O. S. Jones, V. A. Smalyuk, D. T. Casey, A. G. MacPhee, A. Pak, P. M. Celliers, D. S. Clark, O. L. Landen, J. L. Peterson, L. F. Berzak-Hopkins, C. R. Weber, S. W. Haan, T. D. Döppner, S. Dixit, E. Giraldez, A. V. Hamza, K. S. Jancaitis, J. J. Kroll, K. N. Lafortune, B. J. MacGowan, J. D. Moody, A. Nikroo and C. C. Widmayer, Physics of Plasmas **22** (5), 052702 (2015).

40. V. A. Smalyuk, H. F. Robey, T. Döppner, D. T. Casey, D. S. Clark, O. S. Jones, J. L. Milovich, J. L. Peterson, B. Bachmann, K. L. Baker, L. R. Benedetti, L. F. Berzak Hopkins, R. Bionta, E. Bond, D. K. Bradley, D. A. Callahan, P. M. Celliers, C. Cerjan, K.-C. Chen, C. Goyon, G. Grim, S. N. Dixit, M. J. Eckart, M. J. Edwards, M. Farrell, D. N. Fittinghoff, J. A. Frenje, M. Gatu-Johnson, N. Gharibyan, S. W. Haan, A. V. Hamza, E. Hartouni, R. Hatarik, M. Havre, M. Hohenberger, D. Hoover, O. A. Hurricane, N. Izumi, K. S. Jancaitis, S. F. Khan, J. P. Knauer, J. J. Kroll, G. Kyrala, K. N. LaFortune, O. L. Landen, T. Ma, B. J. MacGowan, A. G. MacPhee, M. Mauldin, F. E. Merrill, A. S. Moore, S. Nagel, A. Nikroo, A. Pak, P. K. Patel, J. E. Ralph, D. B. Sayre, D. Shaughnessy, B. K. Spears, R. Tommasini, D. P. Turnbull, A. L. Velikovich, P. L. Volegov, C. R. Weber, C. C. Widmayer and C. Yeamans, Physics of Plasmas **23**, 102703 (2016).

41. A. G. MacPhee, J. L. Peterson, D. T. Casey, D. S. Clark, S. W. Haan, O. S. Jones, O. L. Landen, J. L. Milovich, H. F. Robey and V. A. Smalyuk, Physics of Plasmas **22** (8), 080702 (2015).

42. D. T. Casey, J. L. Milovich, V. A. Smalyuk, D. S. Clark, H. F. Robey, A. Pak, A. G. MacPhee, K. L. Baker, C. R. Weber, T. Ma, H. S. Park, T. Doppner, D. A. Callahan, S. W. Haan, P. K. Patel, J. L. Peterson, D. Hoover, A. Nikroo, C. B. Yeamans, F. E. Merrill, P. L. Volegov, D. N. Fittinghoff, G. P. Grim, M. J. Edwards, O. L. Landen, K. N. Lafortune, B. J. MacGowan, C. C. Widmayer, D. B. Sayre, R. Hatarik, E. J. Bond, S. R. Nagel, L. R. Benedetti, N. Izumi, S. Khan, B. Bachmann, B. K. Spears, C. J. Cerjan, M. Gatu Johnson and J. A. Frenje, Phys Rev Lett **115** (10), 105001 (2015).

43. H. F. Robey, V. A. Smalyuk, J. L. Milovich, T. Döppner, D. T. Casey, K. L. Baker, J. L. Peterson, B. Bachmann, L. F. Berzak Hopkins, E. Bond, J. A. Caggiano, D. A. Callahan, P. M. Celliers, C. Cerjan, D. S. Clark, S. N. Dixit, M. J. Edwards, N. Gharibyan, S. W. Haan, B. A. Hammel, A. V. Hamza, R. Hatarik, O. A. Hurricane, K. S. Jancaitis, O. S. Jones, G. D. Kerbel, J. J. Kroll, K. N. Lafortune, O. L. Landen, T. Ma, M. M. Marinak, B. J. MacGowan, A. G. MacPhee, A. Pak, M. Patel, P. K. Patel, L. J. Perkins, D. B. Sayre, S. M. Sepke, B. K. Spears, R. Tommasini, C. R. Weber, C. C. Widmayer, C. Yeamans, E. Giraldez, D. Hoover, A. Nikroo, M. Hohenberger and M. Gatu Johnson, Physics of Plasmas **23** (5), 056303 (2016).

44. P. Michel, L. Divol, E. A. Williams, C. A. Thomas, D. A. Callahan, S. Weber, S. W. Haan, J. D. Salmonson, N. B. Meezan, O. L. Landen, S. Dixit, D. E. Hinkel, M. J. Edwards, B. J. MacGowan, J. D. Lindl, S. H. Glenzer and L. J. Suter, Physics of Plasmas **16** (4), 042702 (2009).

45. E. L. Dewald, J. Milovich, C. Thomas, J. Kline, C. Sorce, S. Glenn and O. L. Landen, Physics of Plasmas **18** (9), 092703 (2011).

46. J. D. Lindl, P. Amendt, R. L. Berger, S. G. Glendinning, S. H. Glenzer, S. W. Haan, R. L. Kauffman, O. L. Landen and L. J. Suter, Physics of Plasmas **11** (2), 339-491 (2004).

47. E. L. Dewald, D. S. Clark, D. T. Casey, S. F. Khan, D. Mariscal, P. D. Nicola, B. J. MacGowan, E. P. Hartouni, M. S. Rubery, C. Choate, A. Nikroo, V. A. Smalyuk, O. L. Landen, M. Ratledge, P. Fitzsimmons, M. Farrell, M. Mauldin and N. Rice, Physics of Plasmas **29** (9), 092703 (2022).

48. M. M. Marinak, G. D. Kerbel, N. A. Gentile, O. Jones, D. Munro, S. Pollaine, D. T. R and S. W. Haan, Phys. Plasmas **8**, 2275-2280 (2001).

49. D. P. Higginson, D. J. Strozzi, D. Bailey, S. A. MacLaren, N. B. Meezan, S. C. Wilks and G. Zimmerman, Phys. Plasmas **29** (7), 072714 (2022).

50. D. E. Hinkel, L. F. Berzak Hopkins, T. Ma, J. E. Ralph, F. Albert, L. R. Benedetti, P. M. Celliers, T. Doppner, C. S. Goyon, N. Izumi, L. C. Jarrott, S. F. Khan, J. L. Kline, A. L. Kritcher, G. A. Kyrala, S. R. Nagel, A. E. Pak, P. Patel, M. D. Rosen, J. R. Rygg, M. B. Schneider, D. P. Turnbull, C. B. Yeamans, D. A. Callahan and O. A. Hurricane, Phys Rev Lett **117** (22), 225002 (2016).

51. L. Berzak Hopkins, S. Lepape, L. Divol, A. Pak, E. L. Dewald, D. D. D. Ho, N. B. Meezan, S. Bhandarkar, L. R. R. Benedetti, T. Bunn, J. Biener, J. Crippen, D. Casey, D. S. Clark, D. H. Edgell, D. N. Fittinghoff, M. Gatu-Johnson, C. Goyon, S. W. Haan, R. Hatarik, M. Havre, D. Hinkel, H. Huang, N. Izumi, J. Jaquez, O. Jones, S. Khan, A. L. Kritcher, C. Kong, G. Kyrala, O. L. Landen, T. Ma, A. G. MacPhee, B. Macgowan, A. J. A. J. J. Mackinnon, M. Marinak, J. L. Milovich, M. Millot, P. Michel, A. Moore, S. R. S. R. Nagel, A. Nikroo, P. K. Patel, J. E. Ralph, H. F. Robey, J. S. S. Ross, N. G. G. Rice, S. Sepke, V. A. Smalyuk, P. A. Sterne, D. Strozzi, M. Stadermann, P. L. Volegov, C. R. Weber, C. Wild, C. Yeamans, D. A. Callahan, O. A. Hurricane, R. P. J. R. P. J. J. Town, M. J. J. Edwards, S. L. Pape, L. Divol, A. Pak, E. L. Dewald, D. D. D. Ho, N. B. Meezan, S. Bhandarkar, L. R. R. Benedetti, T. Bunn, J. Biener, J. Crippen, D. Casey, D. S. Clark, D. H. Edgell, D. N. Fittinghoff, M. G. Johnson, C. Goyon, S. W. Haan, R. Hatarik, M. Havre, D. Hinkel, H. Huang, N. Izumi, J. Jaquez, O. Jones, S. Khan, A. L. Kritcher, C. Kong, G. Kyrala, O. L. Landen, T. Ma, A. G. MacPhee, B. Macgowan, A. J. A. J. J. Mackinnon, M. Marinak, J. L. Milovich, m. millot, P. Michel, A. Moore, S. R. S. R. Nagel, A. Nikroo, P. K. Patel, J. E. Ralph, H. F. Robey, S. Ross, N. G. G. Rice, S. Sepke, V. A. Smalyuk, P. A. Sterne, D. Strozzi, M. Stadermann, P. L. Volegov, C. R. Weber, C. Wild, C. Yeamans, D. A. Callahan, O. A. Hurricane, R. P. J. R. P. J. J. Town, M. J. J. Edwards, S. Lepape, L. Divol, A. Pak, E. L. Dewald, D. D. D. Ho, N. B. Meezan, S. Bhandarkar, L. R. R. Benedetti, T. Bunn, J. Biener, J. Crippen, D. Casey, D. S. Clark, D. H. Edgell, D. N. Fittinghoff, M.

Gatu-Johnson, C. Goyon, S. W. Haan, R. Hatarik, M. Havre, D. Hinkel, H. Huang, N. Izumi, J. Jaquez, O. Jones, S. Khan, A. L. Kritcher, C. Kong, G. Kyrala, O. L. Landen, T. Ma, A. G. MacPhee, B. Macgowan, A. J. A. J. J. Mackinnon, M. Marinak, J. L. Milovich, M. Millot, P. Michel, A. Moore, S. R. S. R. Nagel, A. Nikroo, P. K. Patel, J. E. Ralph, H. F. Robey, J. S. S. Ross, N. G. G. Rice, S. Sepke, V. A. Smalyuk, P. A. Sterne, D. Strozzi, M. Stadermann, P. L. Volegov, C. R. Weber, C. Wild, C. Yeamans, D. A. Callahan, O. A. Hurricane, R. P. J. R. P. J. J. Town and M. J. J. Edwards, Plasma Physics and Controlled Fusion **61**, 014023 (2018).

52. O. L. Landen, J. Edwards, S. W. Haan, H. F. Robey, J. Milovich, B. K. Spears, S. V. Weber, D. S. Clark, J. D. Lindl, B. J. MacGowan, E. I. Moses, J. Atherton, P. A. Amendt, T. R. Boehly, D. K. Bradley, D. G. Braun, D. A. Callahan, P. M. Celliers, G. W. Collins, E. L. Dewald, L. Divol, J. A. Frenje, S. H. Glenzer, A. Hamza, B. A. Hammel, D. G. Hicks, N. Hoffman, N. Izumi, O. S. Jones, J. D. Kilkenny, R. K. Kirkwood, J. L. Kline, G. A. Kyrala, M. M. Marinak, N. Meezan, D. D. Meyerhofer, P. Michel, D. H. Munro, R. E. Olson, A. Nikroo, S. P. Regan, L. J. Suter, C. A. Thomas and D. C. Wilson, Physics of Plasmas **18** (5), 051002 (2011).

53. P. M. Celliers, D. K. Bradley, G. W. Collins, D. G. Hicks, T. R. Boehly and W. J. Armstrong, Review of Scientific Instruments **75** (11), 4916-4929 (2004).

54. H. F. Robey, P. M. Celliers, J. L. Kline, A. J. Mackinnon, T. R. Boehly, O. L. Landen, J. H. Eggert, D. Hicks, S. Le Pape, D. R. Farley, M. W. Bowers, K. G. Krauter, D. H. Munro, O. S. Jones, J. L. Milovich, D. Clark, B. K. Spears, R. P. Town, S. W. Haan, S. Dixit, M. B. Schneider, E. L. Dewald, K. Widmann, J. D. Moody, T. D. Doppner, H. B. Radousky, A. Nikroo, J. J. Kroll, A. V. Hamza, J. B. Horner, S. D. Bhandarkar, E. Dzenitis, E. Alger, E. Giraldez, C. Castro, K. Moreno, C. Haynam, K. N. LaFortune, C. Widmayer, M. Shaw, K. Jancaitis, T. Parham, D. M. Holunga, C. F. Walters, B. Haid, T. Malsbury, D. Trummer, K. R. Coffee, B. Burr, L. V. Berzins, C. Choate, S. J. Brereton, S. Azevedo, H. Chandrasekaran, S. Glenzer, J. A. Caggiano, J. P. Knauer, J. A. Frenje, D. T. Casey, M. G. Johnson, F. H. Seguin, B. K. Young, M. J. Edwards, B. M. Van Wonterghem, J. Kilkenny, B. J. MacGowan, J. Atherton, J. D. Lindl, D. D. Meyerhofer and E. Moses, Phys Rev Lett **108** (21), 215004 (2012).

55. H. F. Robey, T. R. Boehly, P. M. Celliers, J. H. Eggert, D. Hicks, R. F. Smith, R. Collins, M. W. Bowers, K. G. Krauter, P. S. Datte, D. H. Munro, J. L. Milovich, O. S. Jones, P. A. Michel, C. A. Thomas, R. E. Olson, S. Pollaine, R. P. J. Town, S. Haan, D. Callahan, D. Clark, J. Edwards, J. L. Kline, S. Dixit, M. B. Schneider, E. L. Dewald, K. Widmann, J. D. Moody, T. Döppner, H. B. Radousky, A. Throop, D. Kalantar, P. DiNicola, A. Nikroo, J. J. Kroll, A. V. Hamza, J. B. Horner, S. D. Bhandarkar, E. Dzenitis, E. Alger, E. Giraldez, C. Castro, K. Moreno, C. Haynam, K. N. LaFortune, C. Widmayer, M. Shaw, K. Jancaitis, T. Parham, D. M. Holunga, C. F. Walters, B. Haid, E. R. Mapoles, J. Sater, C. R. Gibson, T. Malsbury, J. Fair, D. Trummer, K. R. Coffee, B. Burr, L. V. Berzins, C. Choate, S. J. Brereton, S. Azevedo, H. Chandrasekaran, D. C. Eder, N. D. Masters, A. C. Fisher, P. A. Sterne, B. K. Young, O. L. Landen, B. M. Van Wonterghem, B. J. MacGowan, J. Atherton, J. D. Lindl, D. D. Meyerhofer and E. Moses, Physics of Plasmas **19** (4), 042706 (2012).

56. D. H. Munro, P. M. Celliers, G. W. Collins, D. M. Gold, L. B. Da Silva, S. W. Haan, R. C. Cauble, B. A. Hammel and W. W. Hsing, Physics of Plasmas **8**, 2245-2250 (2001).

57. P. M. Celliers, H. F. Robey, T. R. Boehly, E. Alger, S. Azevedo, L. V. Berzins, S. D. Bhandarkar, M. W. Bowers, S. J. Brereton, D. Callahan, C. Castro, H. Chandrasekaran, C. Choate, D. S. Clark, K. R. Coffee, P. S. Datte, E. L. Dewald, P. Dinicola, S. Dixit, T. Döppner, E. Dzenitis, M. J. Edwards, J. H. Eggert, J. Fair, D. R. Farley, G. Frieders, C. R. Gibson, E. Giraldez, S. Haan, B. Haid, A. V. Hamza, C. Haynam, D. G. Hicks, D. M. Holunga, J. B. Horner, K. Jancaitis, O. S. Jones, D. Kalantar, J. L. Kline, K. G. Krauter, J. J. Kroll, K. N. Lafortune, S. L. Pape, T. Malsbury, E. R. Mapoles, N. B. Meezan, J. L. Milovich, J. D. Moody, K. Moreno, D. H. Munro, A. Nikroo, R. E. Olson, T. Parham, S. Pollaine, H. B. Radousky, G. F. Ross, J. Sater, M. B. Schneider, M. Shaw, R. F. Smith, P. A. Sterne, C. A. Thomas, A. Throop, R. P. J. Town, D. Trummer, B. M. Van Wonterghem, C. F. Walters, K. Widmann, C. Widmayer, B. K. Young, L. J. Atherton, G. W. Collins, O. L. Landen, J. D. Lindl, B. J. Macgowan, D. D. Meyerhofer and E. I. Moses, EPJ Web of Conferences **59**, 02004 (2013).

58. G. A. Kyrala, J. L. Kline, S. Dixit, S. Glenzer, D. Kalantar, D. Bradley, N. Izumi, N. Meezan, O. Landen, D. Callahan, S. V. Weber, J. P. Holder, S. Glenn, M. J. Edwards, J. Koch, L. J. Suter, S. W. Haan, R. P. J. Town,

P. Michel, O. Jones, S. Langer, J. D. Moody, E. L. Dewald, T. Ma, J. Ralph, A. Hamza, E. Dzenitis and J. Kilkenny, Physics of Plasmas **18** (5), 056307 (2011).

59. J. R. Rygg, O. S. Jones, J. E. Field, M. A. Barrios, L. R. Benedetti, G. W. Collins, D. C. Eder, M. J. Edwards, J. L. Kline, J. J. Kroll, O. L. Landen, T. Ma, A. Pak, J. L. Peterson, K. Raman, R. P. J. Town and D. K. Bradley, Physical Review Letters **112**, 195001 (2014).

60. N. Izumi, N. B. Meezan, S. Johnson, B. N. Woodworth, T. Woods, O. S. Jones, O. L. Landen, J. J. Kroll, S. Vonhof, A. Nikroo, J. Jaquez, K. Kangas, C. Bailey, M. Hardy, R. Ehrlich, J. Ralph, R. P. Town, D. K. Bradley, D. E. Hinkel, A. S. Moore, L. Divol, C. Young and J. D. Moody, Rev Sci Instrum **89** (10), 10K111 (2018).

61. E. L. Dewald, K. M. Campbell, R. E. Turner, J. P. Holder, O. L. Landen, S. H. Glenzer, R. L. Kauffman, L. J. Suter, M. Landon, M. Rhodes and D. Lee, Review of Scientific Instruments **75** (10), 3759-3761 (2004).

62. D. H. Froula, D. Bower, M. Chrisp, S. Grace, J. H. Kamperschroer, T. M. Kelleher, R. K. Kirkwood, B. MacGowan, T. McCarville, N. Sewall, F. Y. Shimamoto, S. J. Shiromizu, B. Young and S. H. Glenzer, Review of Scientific Instruments **75** (10), 4168-4170 (2004).

63. L. J. Suter, A. R. Thiessen, F. Ze, R. Kauffman, R. H. Price, V. C. Rupert, V. W. Slivinsky and C. Wang, Review of Scientific Instruments **68** (1), 838-841 (1997).

64. J. L. Milovich, D. C. Casey, B. MacGowan, D. Clark, D. Mariscal, T. Ma, K. Baker, R. Bionta, K. Hahn, A. Moore, D. Schlossberg, E. Hartouni, S. Sepke and O. Landen, Plasma Physics and Controlled Fusion **63** (025012), 025012 (2021).

65. E. L. L. Dewald, K. M. M. Campbell, R. E. E. Turner, J. P. P. Holder, O. L. L. Landen, S. H. H. Glenzer, R. L. L. Kauffman, L. J. J. Suter, M. Landen, M. Rhodes, D. Lee, M. Landon, M. Rhodes and D. Lee, Rev. Sci. Instrum. **74**, 3759 (2004).

66. N. B. Meezan, D. G. Hicks, D. A. Callahan, R. E. Olson, M. S. Schneider, C. A. Thomas, H. F. Robey, P. M. Celliers, J. L. Kline, S. N. Dixit, P. A. Michel, O. S. Jones, D. S. Clark, J. E. Ralph, T. Döppner, A. J.

Mackinnon, S. W. Haan, O. L. Landen, S. H. Glenzer, L. J. Suter, M. J. Edwards, B. J. Macgowan, J. D. Lindl and L. J. Atherton, EPJ Web of Conferences **59**, 02002 (2013).

67. E. L. Dewald, J. L. Milovich, P. Michel, O. L. Landen, J. L. Kline, S. Glenn, O. Jones, D. H. Kalantar, A. Pak, H. F. Robey, G. A. Kyrala, L. Divol, L. R. Benedetti, J. Holder, K. Widmann, A. Moore, M. B. Schneider, T. Doppner, R. Tommasini, D. K. Bradley, P. Bell, B. Ehrlich, C. A. Thomas, M. Shaw, C. Widmayer, D. A. Callahan, N. B. Meezan, R. P. Town, A. Hamza, B. Dzenitis, A. Nikroo, K. Moreno, B. Van Wonterghem, A. J. Mackinnon, S. H. Glenzer, B. J. MacGowan, J. D. Kilkenny, M. J. Edwards, L. J. Atherton and E. I. Moses, Phys Rev Lett **111** (23), 235001 (2013).

68. J. L. Milovich, E. L. Dewald, A. Pak, P. Michel, R. P. J. Town, D. K. Bradley, O. Landen and M. J. Edwards, Physics of Plasmas **23**, 032701 (2016).

69. M. Basko, Physics of Plasmas **3** (11), 4148-4155 (1996).

70. A. G. MacPhee, V. A. Smalyuk, O. L. Landen, C. R. Weber, H. F. Robey, E. L. Alfonso, K. L. Baker, L. F. Berzak Hopkins, J. Biener, T. Bunn, D. T. Casey, D. S. Clark, J. W. Crippen, L. Divol, M. Farrell, S. Felker, J. E. Field, W. W. Hsing, C. Kong, S. Le Pape, D. A. Martinez, P. Michel, J. Milovich, A. Moore, A. Nikroo, L. Pickworth, N. Rice, M. Stadermann, C. Yeamans and C. Wild, Phys. Plasmas **25** (8) (2018).

71. M. M. Marinak, B. A. Remington, S. V. Weber, R. E. Tipton, S. W. Haan, K. S. Budil, O. L. Landen, J. D. Kilkenny and R. Wallace, Physical Review Letters **75**, 3677 (1995).

72. A. L. Kritcher, J. Ralph, D. E. Hinkel, T. Döppner, M. Millot, D. Mariscal, R. Benedetti, D. J. Strozzi, T. Chapman, C. Goyon, B. Macgowan, P. Michel, D. A. Callahan and O. A. Hurricane, Physical Review E **98**, 053206 (2018).

73. L. A. Pickworth, T. Döppner, D. E. Hinkel, J. E. Ralph, B. Bachmann, L. P. Masse, L. Divol, L. R. Benedetti, P. M. Celliers, H. Chen, M. Hohenberger, S. F. Khan, O. L. Landen, N. Lemos, B. J. MacGowan, D. A. Mariscal, P. A. Michel, M. Millot, A. S. Moore, J. Park, M. B. Schneider, D. A. Callahan and O. A. Hurricane, Physics of Plasmas **27** (10), 102702 (2020).

74. J. D. Moody, P. Michel, L. Divol, R. L. Berger, E. Bond, D. K. Bradley, D. A. Callahan, E. L. Dewald, S. Dixit, M. J. Edwards, S. Glenn, A. Hamza, C. Haynam, D. E. Hinkel, N. Izumi, O. Jones, J. D. Kilkenny, R. K. Kirkwood, J. L. Kline, W. L. Kruer, G. A. Kyrala, O. L. Landen, S. LePape, J. D. Lindl, B. J. MacGowan, N. B. Meezan, A. Nikroo, M. D. Rosen, M. B. Schneider, D. J. Strozzi, L. J. Suter, C. A. Thomas, R. P. J. Town, K. Widmann, E. A. Williams, L. J. Atherton, S. H. Glenzer and E. I. Moses, Nature Physics **8** (4), 344-349 (2012).

75. P. Michel, L. Divol, R. P. Town, M. D. Rosen, D. A. Callahan, N. B. Meezan, M. B. Schneider, G. A. Kyrala, J. D. Moody, E. L. Dewald, K. Widmann, E. Bond, J. L. Kline, C. A. Thomas, S. Dixit, E. A. Williams, D. E. Hinkel, R. L. Berger, O. L. Landen, M. J. Edwards, B. J. MacGowan, J. D. Lindl, C. Haynam, L. J. Suter, S. H. Glenzer and E. Moses, Phys Rev E **83** (4 Pt 2), 046409 (2011).

76. D. A. Callahan, O. A. Hurricane, A. L. Kritcher, D. T. Casey, D. E. Hinkel, Y. P. Opachich, H. F. Robey, M. D. Rosen, J. S. Ross, M. S. Rubery, C. V. Young and A. B. Zylstra, Physics of Plasmas **27** (7), 072704 (2020).

77. T. Döppner, D. A. Callahan, O. A. Hurricane, D. E. Hinkel, T. Ma, H. S. Park, L. F. Berzak Hopkins, D. T. Casey, P. Celliers, E. L. Dewald, T. R. Dittrich, S. W. Haan, A. L. Kritcher, A. MacPhee, S. Le Pape, A. Pak, P. K. Patel, P. T. Springer, J. D. Salmonson, R. Tommasini, L. R. Benedetti, E. Bond, D. K. Bradley, J. Caggiano, J. Church, S. Dixit, D. Edgell, M. J. Edwards, D. N. Fittinghoff, J. Frenje, M. Gatu Johnson, G. Grim, R. Hatarik, M. Havre, H. Herrmann, N. Izumi, S. F. Khan, J. L. Kline, J. Knauer, G. A. Kyrala, O. L. Landen, F. E. Merrill, J. Moody, A. S. Moore, A. Nikroo, J. E. Ralph, B. A. Remington, H. F. Robey, D. Sayre, M. Schneider, H. Streckert, R. Town, D. Turnbull, P. L. Volegov, A. Wan, K. Widmann, C. H. Wilde and C. Yeamans, Phys Rev Lett **115** (5), 055001 (2015).

78. O. S. Jones, C. J. Cerjan, M. M. Marinak, J. L. Milovich, H. F. Robey, P. T. Springer, L. R. Benedetti, D. L. Bleuel, E. J. Bond, D. K. Bradley, D. A. Callahan, J. A. Caggiano, P. M. Celliers, D. S. Clark, S. M. Dixit, T. Doppner, R. J. Dylla-Spears, E. G. Dzentitis, D. R. Farley, S. M. Glenn, S. H. Glenzer, S. W. Haan, B. J. Haid, C. A. Haynam, D. G. Hicks, B. J. Kozioziemski, K. N. Lafortune, O. L. Landen, E. R. Mapoles, A. J. MacKinnon, J. M. McNaney, N. B. Meezan, P. A. Michel, J. D. Moody, M. J. Moran, D. H. Munro, M. V. Patel, T. G.

Parham, J. D. Sater, S. M. Sepke, B. K. Spears, R. P. J. Town, S. V. Weber, K. Widmann, C. C. Widmayer, E. A. Williams, L. J. Atherton, M. J. Edwards, J. D. Lindl, B. J. MacGowan, L. J. Suter, R. E. Olson, H. W. Herrmann, J. L. Kline, G. A. Kyrala, D. C. Wilson, J. Frenje, T. R. Boehly, V. Glebov, J. P. Knauer, A. Nikroo, H. Wilkens and J. D. Kilkenny, Physics of Plasmas **19**, 056315 (2012).

79. S. A. MacLaren, M. B. Schneider, K. Widmann, J. H. Hammer, B. E. Yoxall, J. D. Moody, P. M. Bell, L. R. Benedetti, D. K. Bradley, M. J. Edwards, T. M. Guymer, D. E. Hinkel, W. W. Hsing, M. L. Kervin, N. B. Meezan, A. S. Moore and J. E. Ralph, Phys. Rev. Lett. **112**, 105003 (2014).

80. E. L. Dewald, C. Thomas, S. Hunter, L. Divol, N. Meezan, S. H. Glenzer, L. J. Suter, E. Bond, J. L. Kline, J. Celeste, D. Bradley, P. Bell, R. L. Kauffman, J. Kilkenny and O. L. Landen, Rev Sci Instrum **81** (10), 10D938 (2010).

81. R. Tommasini, O. L. Landen, L. Berzak Hopkins, S. P. Hatchett, D. H. Kalantar, W. W. Hsing, D. A. Alessi, S. L. Ayers, S. D. Bhandarkar, M. W. Bowers, D. K. Bradley, A. D. Conder, J. M. Di Nicola, P. Di Nicola, L. Divol, D. Fittinghoff, G. Gururangan, G. N. Hall, M. Hamamoto, D. R. Hargrove, E. P. Hartouni, J. E. Heebner, S. I. Herriot, M. R. Hermann, J. P. Holder, D. M. Holunga, D. Homoelle, C. A. Iglesias, N. Izumi, A. J. Kemp, T. Kohut, J. J. Kroll, K. LaFortune, J. K. Lawson, R. Lowe-Webb, A. J. MacKinnon, D. Martinez, N. D. Masters, M. P. Mauldin, J. Milovich, A. Nikroo, J. K. Okui, J. Park, M. Prantil, L. J. Pelz, M. Schoff, R. Sigurdsson, P. L. Volegov, S. Vonhof, T. L. Zobrist, R. J. Wallace, C. F. Walters, P. Wegner, C. Widmayer, W. H. Williams, K. Youngblood, M. J. Edwards and M. C. Herrmann, Phys Rev Lett **125** (15), 155003 (2020).

82. B. J. MacGowan, O. L. Landen, D. T. Casey, C. V. Young, D. A. Callahan, E. P. Hartouni, R. Hatarik, M. Hohenberger, T. Ma, D. Mariscal, A. Moore, R. Nora, H. G. Rinderknecht, D. Schlossberg and B. M. Van Wonterghem, High Energy Density Physics **40**, 100944 (2021).

83. N. B. Meezan, A. J. MacKinnon, D. G. Hicks, E. L. Dewald, R. Tommasini, S. Le Pape, T. Döppner, T. Ma, D. R. Farley, D. H. Kalantar, P. Di Nicola, D. A. Callahan, H. F. Robey, C. A. Thomas, S. T. Prisbrey, O. S. Jones, J. L. Milovich, D. S. Clark, D. C. Eder, M. B. Schneider, K. Widmann, J. A. Koch, J. D. Salmonson, Y. P.

Opachich, L. R. Benedetti, S. F. Khan, A. G. MacPhee, S. M. Glenn, D. K. Bradley, E. G. Dzenitis, B. R. Nathan, J. J. Kroll, A. V. Hamza, S. N. Dixit, L. J. Atherton, O. L. Landen, S. H. Glenzer, W. W. Hsing, L. J. Suter, M. J. Edwards, B. J. MacGowan, E. I. Moses, R. E. Olson, J. L. Kline, G. A. Kyrala, A. S. Moore, J. D. Kilkenny, A. Nikroo, K. Moreno and D. E. Hoover, Physics of Plasmas **20** (5), 056311 (2013).

84. A. L. Kritcher, A. B. Zylstra, D. A. Callahan, O. A. Hurricane, C. R. Weber, D. S. Clark, C. V. Young, J. E. Ralph, D. T. Casey, A. Pak, O. L. Landen, B. Bachmann, K. L. Baker, L. Berzak Hopkins, S. D. Bhandarkar, J. Biener, R. M. Bionta, N. W. Birge, T. Braun, T. M. Briggs, P. M. Celliers, H. Chen, C. Choate, L. Divol, T. Döppner, D. Fittinghoff, M. J. Edwards, M. Gatu Johnson, N. Gharibyan, S. Haan, K. D. Hahn, E. Hartouni, D. E. Hinkel, D. D. Ho, M. Hohenberger, J. P. Holder, H. Huang, N. Izumi, J. Jeet, O. Jones, S. M. Kerr, S. F. Khan, H. Geppert Kleinrath, V. Geppert Kleinrath, C. Kong, K. M. Lamb, S. Le Pape, N. C. Lemos, J. D. Lindl, B. J. MacGowan, A. J. Mackinnon, A. G. MacPhee, E. V. Marley, K. Meaney, M. Millot, A. S. Moore, K. Newman, J. M. G. Di Nicola, A. Nikroo, R. Nora, P. K. Patel, N. G. Rice, M. S. Rubery, J. Sater, D. J. Schlossberg, S. M. Sepke, K. Sequoia, S. J. Shin, M. Stadermann, S. Stoupin, D. J. Strozzi, C. A. Thomas, R. Tommasini, C. Trosseille, E. R. Tubman, P. L. Volegov, C. Wild, D. T. Woods and S. T. Yang, Physical Review E **106** (2), 025201 (2022).

85. O. L. Landen, R. Benedetti, D. Bleuel, T. R. Boehly, D. K. Bradley, J. A. Caggiano, D. A. Callahan, P. M. Celliers, C. J. Cerjan, D. Clark, G. W. Collins, E. L. Dewald, S. N. Dixit, T. Doeppner, D. Edgell, J. Eggert, D. Farley, J. A. Frenje, V. Glebov, S. M. Glenn, S. H. Glenzer, S. W. Haan, A. Hamza, B. A. Hammel, C. A. Haynam, J. H. Hammer, R. F. Heeter, H. W. Herrmann, D. G. Hicks, D. E. Hinkel, N. Izumi, M. Gatu Johnson, O. S. Jones, D. H. Kalantar, R. L. Kauffman, J. D. Kilkenny, J. L. Kline, J. P. Knauer, J. A. Koch, G. A. Kyrala, K. LaFortune, T. Ma, A. J. Mackinnon, A. J. Macphee, E. Mapoles, J. L. Milovich, J. D. Moody, N. B. Meezan, P. Michel, A. S. Moore, D. H. Munro, A. Nikroo, R. E. Olson, K. Opachich, A. Pak, T. Parham, P. Patel, H. S. Park, R. P. Petrasso, J. Ralph, S. P. Regan, B. A. Remington, H. G. Rinderknecht, H. F. Robey, M. D. Rosen, J. S. Ross, J. D. Salmonson, T. C. Sangster, M. B. Schneider, V. Smalyuk, B. K. Spears, P. T. Springer, L. J.

Suter, C. A. Thomas, R. P. J. Town, S. V. Weber, P. J. Wegner, D. C. Wilson, K. Widmann, C. Yeamans, A. Zylstra, M. J. Edwards, J. D. Lindl, L. J. Atherton, W. W. Hsing, B. J. MacGowan, B. M. Van Wonterghem and E. I. Moses, Plasma Physics and Controlled Fusion **54** (12), 124026 (2012).

86. V. A. Smalyuk, L. J. Atherton, L. R. Benedetti, R. Bionta, D. Bleuel, E. Bond, D. K. Bradley, J. Caggiano, D. A. Callahan, D. T. Casey, P. M. Celliers, C. J. Cerjan, D. Clark, E. L. Dewald, S. N. Dixit, T. Doppner, D. H. Edgell, M. J. Edwards, J. Frenje, M. Gatu-Johnson, V. Y. Glebov, S. Glenn, S. H. Glenzer, G. Grim, S. W. Haan, B. A. Hammel, E. P. Hartouni, R. Hatarik, S. Hatchett, D. G. Hicks, W. W. Hsing, N. Izumi, O. S. Jones, M. H. Key, S. F. Khan, J. D. Kilkenny, J. L. Kline, J. Knauer, G. A. Kyrala, O. L. Landen, S. Le Pape, J. D. Lindl, T. Ma, B. J. MacGowan, A. J. Mackinnon, A. G. MacPhee, J. McNaney, N. B. Meezan, J. D. Moody, A. Moore, M. Moran, E. I. Moses, A. Pak, T. Parham, H. S. Park, P. K. Patel, R. Petrasso, J. E. Ralph, S. P. Regan, B. A. Remington, H. F. Robey, J. S. Ross, B. K. Spears, P. T. Springer, L. J. Suter, R. Tommasini, R. P. Town, S. V. Weber and K. Widmann, Phys Rev Lett **111** (21), 215001 (2013).

87. O. A. Hurricane, A. Kritcher, D. A. Callahan, O. Landen, P. K. Patel, P. T. Springer, D. T. Casey, E. L. Dewald, T. R. Dittrich, T. Döppner, D. E. Hinkel, L. F. Berzak Hopkins, J. Kline, S. Le Pape, T. Ma, A. G. MacPhee, A. Moore, A. Pak, H. S. Park, J. Ralph, J. D. Salmonson and K. Widmann, Physics of Plasmas **24** (9), 092706 (2017).

88. K. L. Baker, O. Jones, C. Weber, D. Clark, P. K. Patel, C. A. Thomas, O. L. Landen, R. Nora, G. J. Anderson, J. Gaffney, S. MacLaren, D. T. Casey, T. Döppner, E. L. Dewald, R. Tommasini, B. K. Spears, J. Salmonson, M. Hohenberger, S. Khan, A. Zylstra, A. Kritcher, P. Amendt, V. Smalyuk, J. Lindl, C. Young, J. S. Ross, D. Ho, O. A. Hurricane, D. A. Callahan, T. Woods, J. L. Milovich, D. J. Strozzi, B. Bachmann, R. Bionta, P. M. Celliers, D. Fittinghoff, R. Hatarik, M. Gatu Johnson, K. Meaney, M. Millot, P. L. Volegov and C. Wilde, Physics of Plasmas **29** (6), 062705 (2022).

89. P. Amendt, D. Ho, Y. Ping, V. Smalyuk, S. Khan, J. Lindl, D. Strozzi, R. Tommasini, M. Belyaev, C. Cerjan, O. Jones, W. Kruer, N. Meezan, H. Robey, F. Tsung, C. Weber and C. Young, Physics of Plasmas **26** (8), 082707 (2019).

90. B. A. Hammel, C. R. Weber, M. Stadermann, C. L. Alday, C. Aracne-Ruddle, J. R. Bigelow, D. S. Clark, J. P. Cortez, S. Diaz, T. Döppner, S. Felker, J. E. Field, S. W. Haan, M. O. Havre, C. Heinbockel, D. E. Hinkel, W. W. Hsing, S. A. Johnson, A. Nikroo, L. A. Pickworth, J. E. Ralph, H. F. Robey and V. A. Smalyuk, Physics of Plasmas **25** (8), 082714 (2018).

91. J. E. Ralph, T. Döppner, D. E. Hinkel, O. Hurricane, O. Landen, V. Smalyuk, C. R. Weber, J. Bigelow, B. Bachmann, D. T. Casey, D. Clark, S. Diaz, S. Felker, B. A. Hammel, S. F. Khan, A. Nikroo, A. Pak, P. K. Patel, D. A. Callahan, J. Sater, P. Springer, M. Stadermann, C. Walters, M. Havre and P. L. Volegov, Physics of Plasmas **27** (10), 102708 (2020).

92. S. R. Nagel, S. W. Haan, J. R. Rygg, M. Barrios, L. R. Benedetti, D. K. Bradley, J. E. Field, B. A. Hammel, N. Izumi, O. S. Jones, S. F. Khan, T. Ma, A. E. Pak, R. Tommasini and R. P. J. Town, Phys. Plasmas **22** (22704), 22704 (2015).

93. R. Tommasini, J. E. Field, B. A. Hammel, O. L. Landen, S. W. Haan, C. Aracne-Ruddle, L. R. Benedetti, D. K. Bradley, D. A. Callahan, E. L. Dewald, T. Doeppner, M. J. Edwards, O. A. Hurricane, N. Izumi, O. A. Jones, T. Ma, N. B. Meezan, S. R. Nagel, J. R. Rygg, K. S. Segraves, M. Stadermann, R. J. Strauser and R. P. J. Town, Physics of Plasmas **22**, 056315 (2015).

94. T. R. Dittrich, O. A. Hurricane, D. A. Callahan, E. L. Dewald, T. Döppner, D. E. Hinkel, L. F. Berzak Hopkins, S. Le Pape, T. Ma, J. L. Milovich, J. C. Moreno, P. K. Patel, H. S. Park, B. A. Remington, J. D. Salmonson and J. L. Kline, Physical Review Letters **112**, 055002 (2014).

95. S. A. MacLaren, L. P. Masse, C. E. Czajka, S. F. Khan, G. A. Kyrala, T. Ma, J. E. Ralph, J. D. Salmonson, B. Bachmann, L. R. Benedetti, S. D. Bhandarkar, P. A. Bradley, R. Hatarik, H. W. Herrmann, D. A. Mariscal,

M. Millot, P. K. Patel, J. E. Pino, M. Ratledge, N. G. Rice, R. E. Tipton, R. Tommasini and C. B. Yeamans, Physics of Plasmas **25** (5), 056311 (2018).

96. C. R. Weber, D. T. Casey, D. S. Clark, B. A. Hammel, A. MacPhee, J. Milovich, D. Martinez, H. F. Robey, V. A. Smalyuk, M. Stadermann, P. Amendt, S. Bhandarkar, B. Chang, C. Choate, J. Crippen, S. J. Felker, J. E. Field, S. W. Haan, S. Johnson, J. J. Kroll, O. L. Landen, M. Marinak, M. McInnis, A. Nikroo, N. Rice and S. M. Sepke, Physics of Plasmas **24** (5), 056302 (2017).

97. D. C. Wilson, P. A. Bradley, N. M. Hoffman, F. J. Swenson, D. P. Smitherman, R. E. Chrien, R. W. Margevicius, D. J. Thoma, L. R. Foreman, J. K. Hoffer, S. R. Goldman, S. E. Caldwell, T. R. Dittrich, S. W. Haan, M. M. Marinak, S. M. Pollaine and J. J. Sanchez, Physics of Plasmas **5** (5), 1953-1959 (1998).

98. A. L. Kritcher, D. Clark, S. Haan, S. A. Yi, A. B. Zylstra, D. A. Callahan, D. E. Hinkel, L. F. Berzak Hopkins, O. A. Hurricane, O. L. Landen, S. A. MacLaren, N. B. Meezan, P. K. Patel, J. Ralph, C. A. Thomas, R. Town and M. J. Edwards, Physics of Plasmas **25** (5), 056309 (2018).

99. G. Robert, A. Sollier, P. Legrand, M. Elert, M. D. Furnish, R. Chau, N. Holmes and J. Nguyen, AIP Conference Proceedings **955**, 97-100 (2007).

Figure Captions

Figure 1. Hohlraum cross-section schematic showing the inner and outer beams and the important hohlraum dynamics of outer bubble inward radial motion intercepting inner beams and formation of stagnation ridge between capsule and wall blow-off near equator stopping transmitted portion of inner beams.

Figure 2. Illustrative outer cone geometry for the outer beam phasing case at a) t = 0, and at b) t = 6 ns after some inward wall motion. c) Inner quad powers versus time and d) Outer quad powers vs time. For the azimuthal beam phased case, only every other 50° quad is used (denoted 50a) up to 6 ns, at twice the power per 50° quad as shown in black dashed lines on d), then the 50b quads are turned on at 6 ns at the same time as 45° quads.

Figure 3 Illumination patterns at start of picket pulse in unwrapped cylindrical hohlraum wall. 50% intensity contours shown are for 23.5° in red, 30° blue, 44.5° green and 50° black. a) Standard 192 beams, b) Outer Beam Phased case where 45° beams turned off and c) Azimuthal Beam Phased case where every other 50° quad also turned off leaving group denoted 50a.

Figure 4. Total power (solid line), and ratio of inner cone to total power (CF) (dashed line) versus time.

Figure 5. a) Hohlraum schematic, b) Capsule schematic, and c) Laser power profile of current adiabat shaped 4 shock CH design (solid line), compared to a 3-shock HDC design (dashed line). Inset shows picket and trough of adiabat-shaped 4 shock.

Figure 6. Experimental platforms utilized to tune up the low mode drive symmetry. a) interferometric velocimetry setup to observe shock velocity and breakout timing known as “KeyHole”. b) Implosion experiment using a surrogate capsule without DT ice layer called “SymCap”. c) X-ray backlit radiography to measure symmetry and velocity of the shell in-flight at the time close to its maximum velocity timing called “2DConA”.

Figure 7. a) Streaked VISAR trace showing breakout of first shock, and successive shock merges at polar angle = 0, 45, 90° degrees b) Comparison of equatorial shock speeds for current low gas-fill design (black bars) and high gas-fill design (gray bars). c) Legendre decomposition of the shock breakout (black bars) and 1-2 merge times (open bars) of current design.

Figure 8. a) and b) are multi-keV gated x-ray images at various times through top LEH and c) and d) are lineouts through a bubble tip without and with the use of the azimuthal beam phasing technique.

Figure 9. Radii of the bubble tips and troughs and laser power profiles versus time. a) Comparison of bubble tip trajectory obtained without azimuthal beam phasing on a SymCap shot (black circles) and

KeyHole shot (red circles). Gray band denotes extent of inner beams at bubble tip plane. b) Bubble growth trajectory of SymCap and KeyHole overlaid by referencing to final rise time. Closed circles are without azimuthal beam phasing, and open circles are radii of the bubble tip and trough with azimuthal beam phasing. Dashed line at 2.875 mm shows the initial radius of the hohlraum wall.

Figure 10. a) Ray trace showing expected position of inner cone energy deposition at peak power seen from $\theta = 90°$, $\phi = 79°$ line of sight. The square region shown by the yellow box is the extent of the thin-wall Au patch (nominal thickness of 8 μm). The inner cone beams are shown emitting at an expected density ridge located at r = 2.1 mm. On this line-of-sight, the front and rear spots of the 23.5° quads (red dots) and 30° quads (blue dots) are almost aligned on the top side of the hohlraum as shown in b) bubble image from top side LEH on N220222 without ABP and c) bubble image of N211229 with ABP. d) and e) are X--ray images obtained through the thin-wall for shots without and with ABP. After compensation of the x-ray signal attenuation through the measured thicknesses of the thin-wall patches, d) and e) are shown using the same gray scale so that we can directly compare the relative brightness between them.

Figure 11. Equatorial X-ray core images with and without ABP as functions of wavelength separation $\Delta\lambda$ (@ 1ω) between inner and outer cone beams. Legendre amplitudes of low mode distortion of the imploded core versus $\Delta\lambda$. P_2 (P_4) amplitude is shown by circles (squares). Solid points are without ABP, open points employ ABP.

Figure 12. Time integrated X-ray images from the same equatorial view as Figure 8 for $\Delta\lambda$ = 0 and 1 Å. wavelength separation. Below each figure the ratio of x-ray intensities of the 30° to 23.5° quads is given. After compensation of the x-ray signal attenuation through the measured thicknesses of the thin-wall patches, a) and b) are shown using the same gray scale so that we can directly compare the relative brightness between them.

Figure 13. Average time-integrated hard x-ray emissivity through thin-wall patches corrected for wall thickness and curvature, versus measured core P_2 asymmetry. Open and closed circles are with and without ABP, respectively.

Figure 14. Energy in 50° cone SBS (closed circles), 30° cone SBS (open circles) and 30° cone SRS (open squares) as a function of wavelength separation at 1ω between the inner and outer beams.

Figure 15. a) 6 keV X-ray backlit images of imploding capsule. b) Limb minimum average radius versus time with linear fit. c) Legendre mode 2 (closed circles) and 4 (open squares) of limb minimum versus time, the values of the Legendre modes at 15.2 ns correspond to the analysis of the 17% contour of the x-ray core self-emission image.

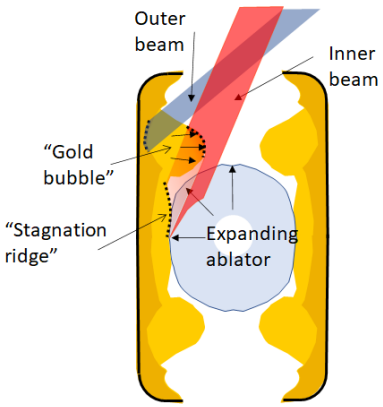
Outer
beam
Inner
beam
"Gold
bubble"
"Stagnation
ridge"
Expanding
ablator

Figure 1

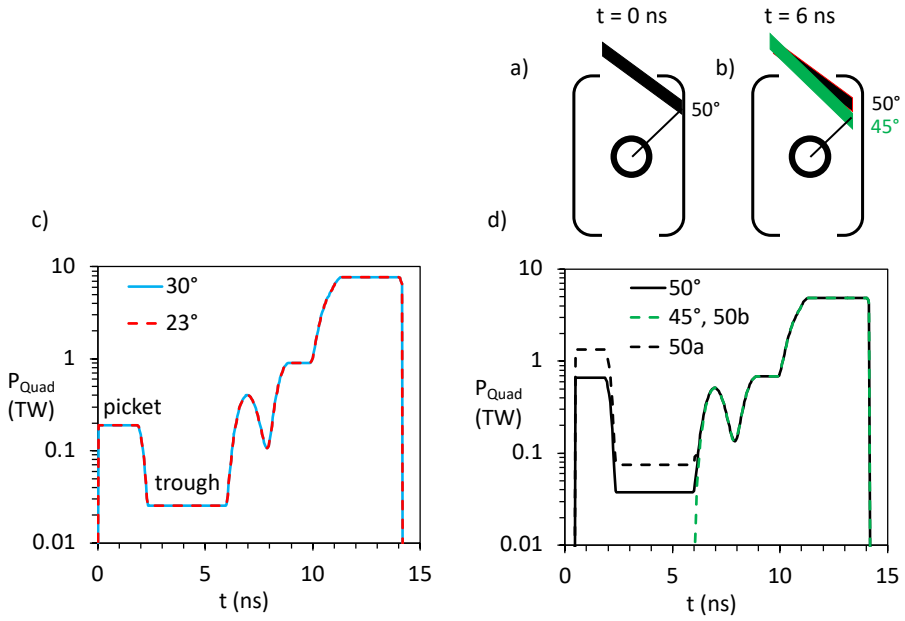
t = 0 ns
t = 6 ns
a)
b)
50°
50°
45°
c)
d)
10
1
0.1
0.01
P_Quad (TW)
30°
23°
picket
trough
0
5
10
15
t (ns)
50°
45°, 50b
50a

Figure 2

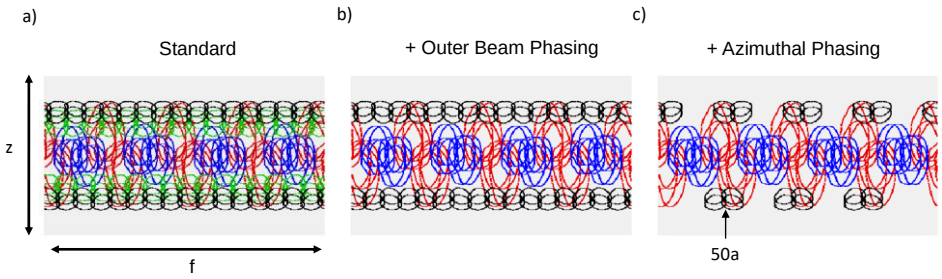

Figure 3

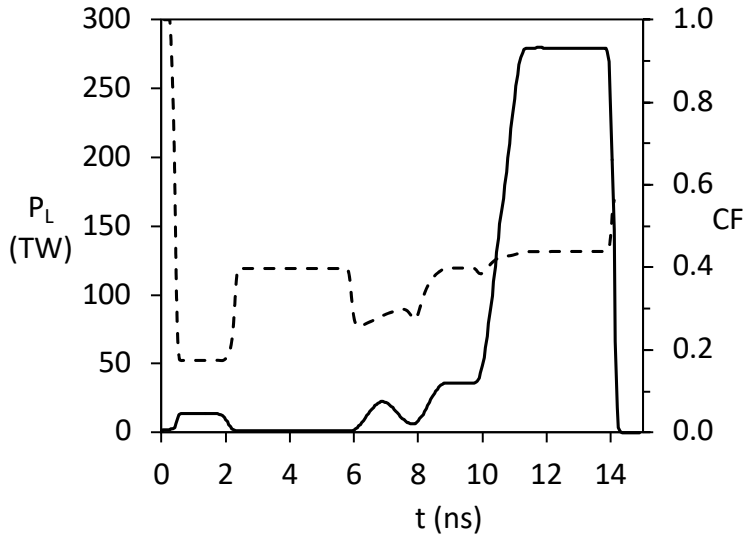
300
250
200
150
100
50
0
P_L
(TW)
1.0
0.8
0.6
0.4
0.2
0.0
CF
0
2
4
6
8
10
12
14
t (ns)

Figure 4

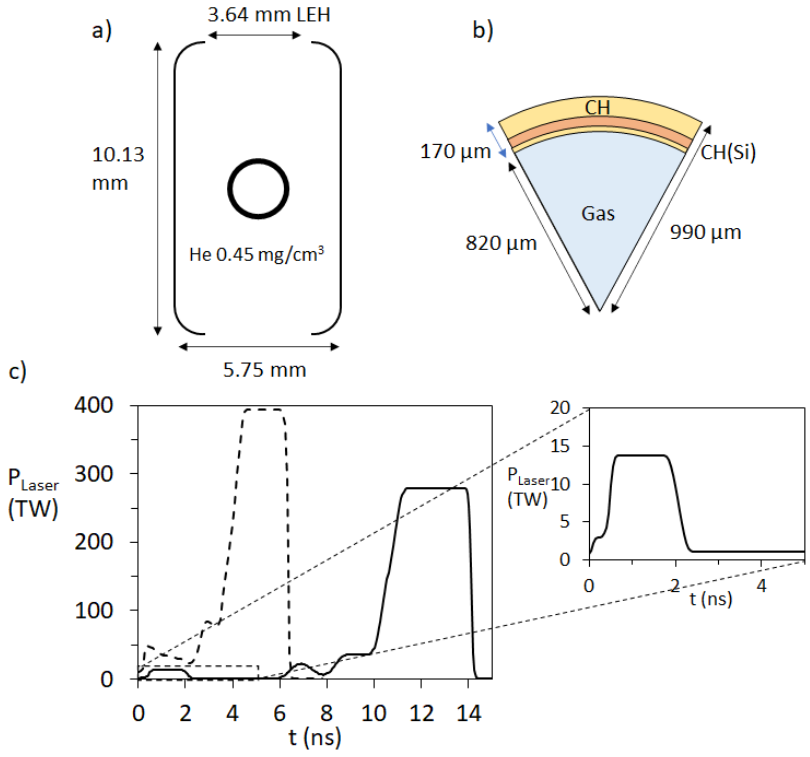
a)
3.64 mm LEH
10.13 mm
He 0.45 mg/cm³
5.75 mm
b)
CH
170 µm
CH(Si)
Gas
820 µm
990 µm
c)
P_Laser (TW)
400
300
200
100
0
0 2 4 6 8 10 12 14
t (ns)
20
15
10
5
0
0 2 4
t (ns)

Figure 5

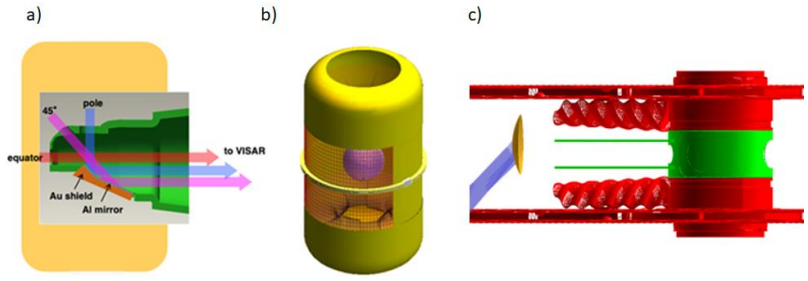

Figure 6

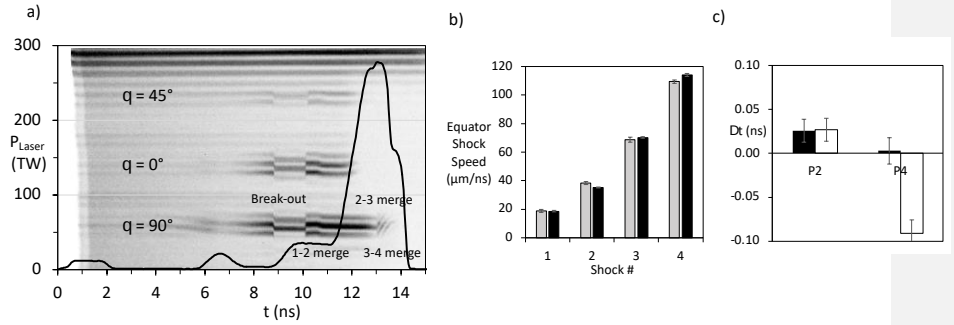
a)
b)
c)
300
200
100
0
P_Laser (TW)
q = 45°
q = 0°
q = 90°
Break-out
2-3 merge
1-2 merge
3-4 merge
0 2 4 6 8 10 12 14
t (ns)
120
100
80
60
40
20
0
Equator Shock Speed (μm/ns)
1 2 3 4
Shock #
0.10
0.05
0.00
-0.05
-0.10
Dt (ns)
P2
P4

Figure 7

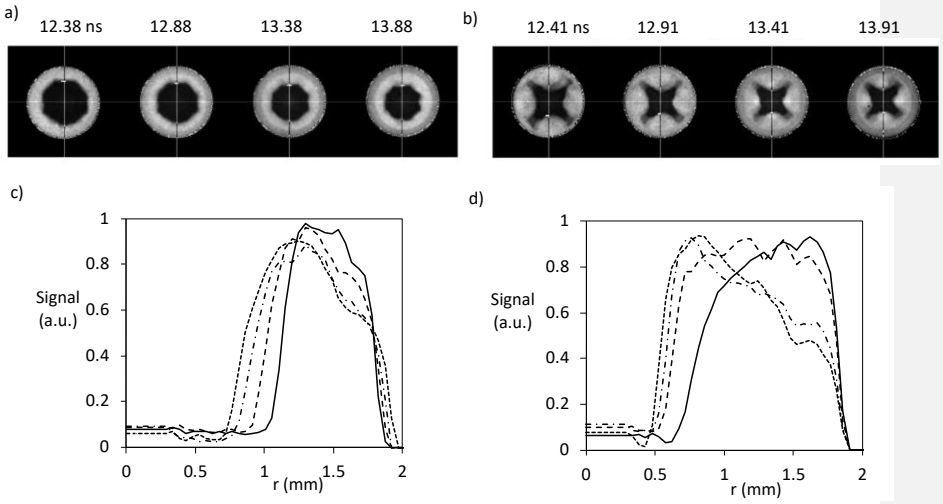
a)
12.38 ns
12.88
13.38
13.88
b)
12.41 ns
12.91
13.41
13.91
c)
Signal (a.u.)
r (mm)
d)
Signal (a.u.)
r (mm)

Figure 8

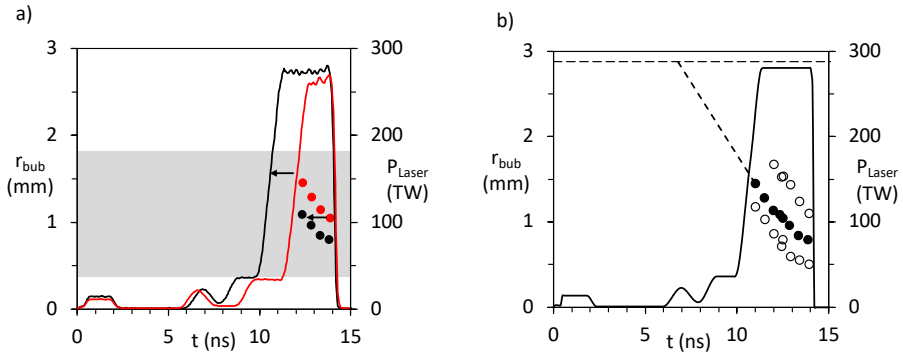

Figure 9

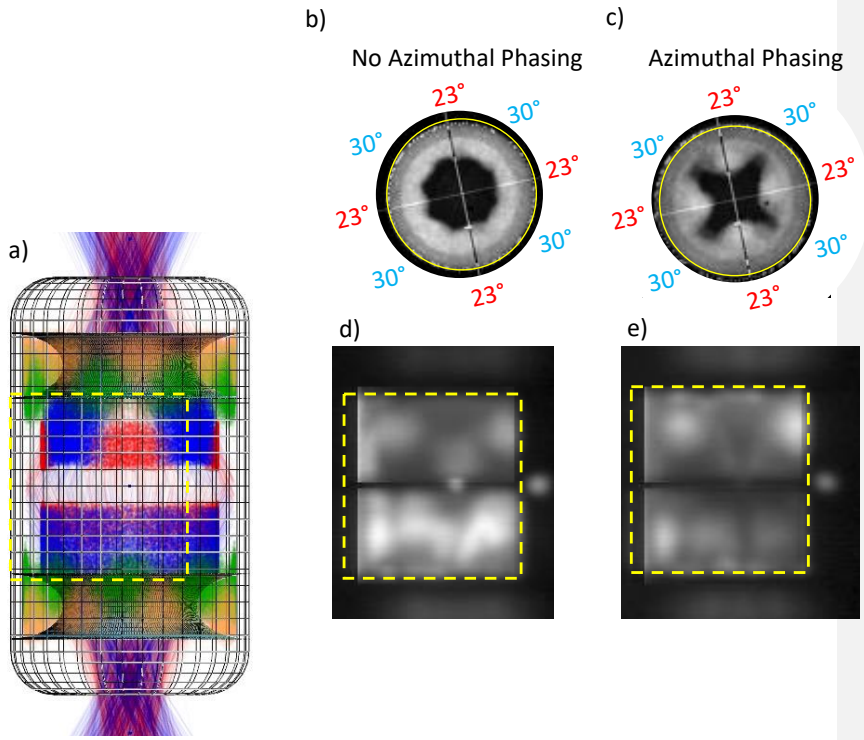
a)
b)
No Azimuthal Phasing
23°
30°
30°
23°
23°
30°
30°
23°
c)
Azimuthal Phasing
23°
30°
30°
23°
23°
30°
30°
23°
d)
e)

Figure 10

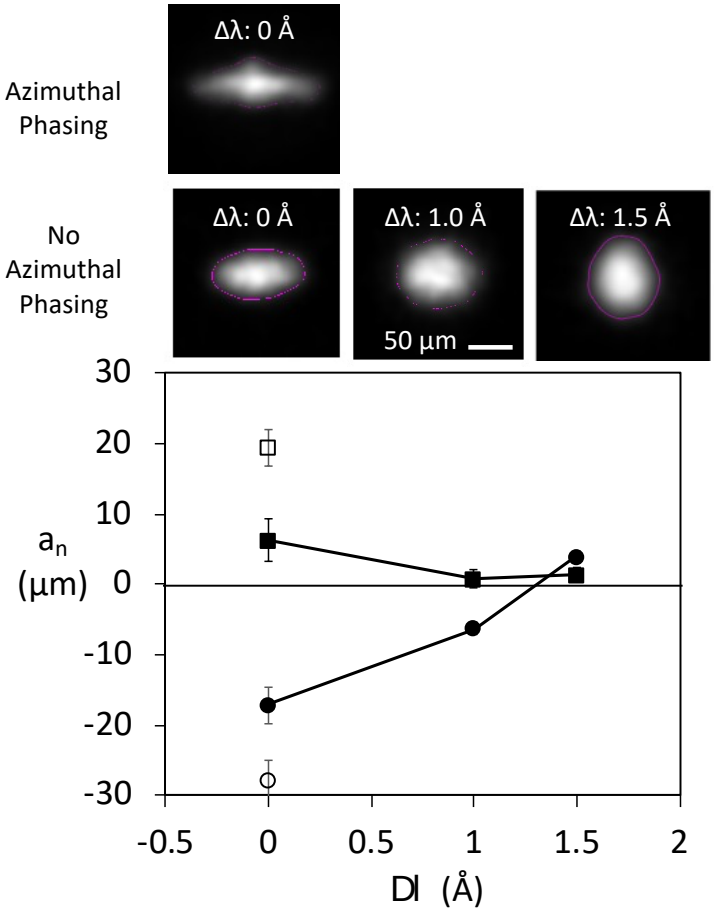
Δλ: 0 Å
Azimuthal Phasing
Δλ: 0 Å
Δλ: 1.0 Å
Δλ: 1.5 Å
No Azimuthal Phasing
50 µm
30
20
10
0
-10
-20
-30
a_n (µm)
-0.5
0
0.5
1
1.5
2
Dl (Å)

Figure 11

a) Dl = 0 Å b) Dl = 1 Å

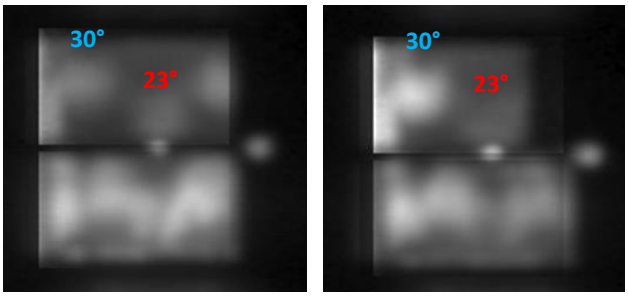

30°/23° = 1.4 30°/23° = 5.5

Figure 12

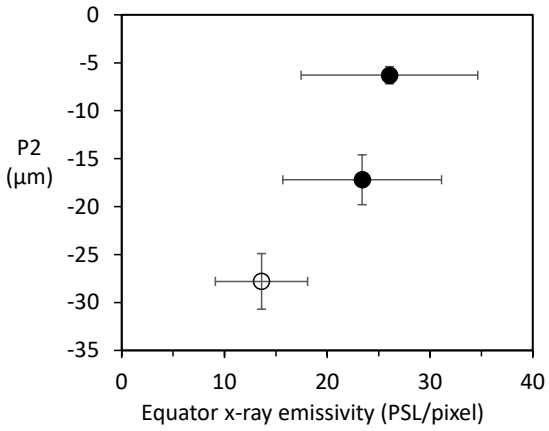
0
-5
-10
-15
-20
-25
-30
-35
P2
(μm)
0
10
20
30
40
Equator x-ray emissivity (PSL/pixel)

Figure 13

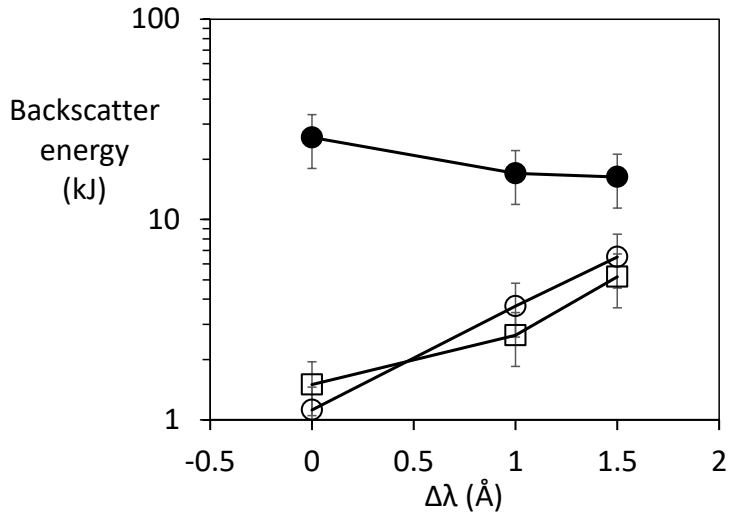

Figure 14

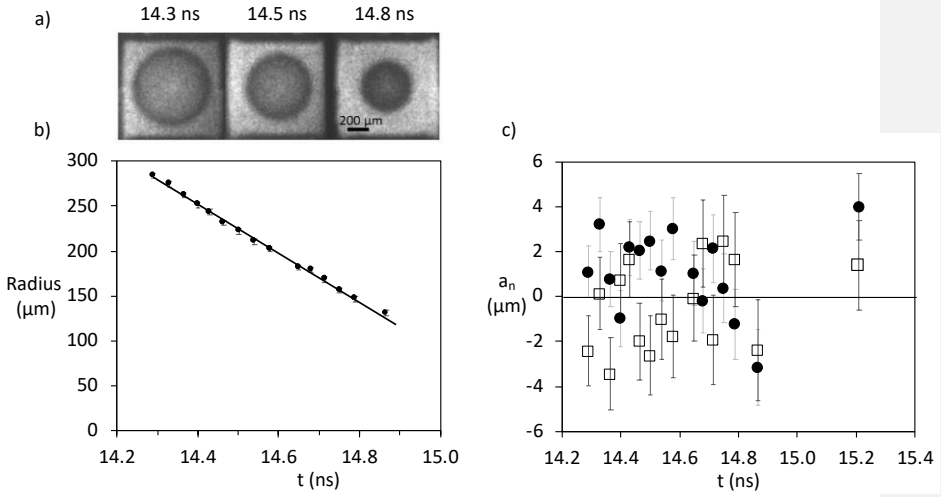
a)
14.3 ns
14.5 ns
14.8 ns
200 µm
b)
Radius (µm)
300
250
200
150
100
50
0
14.2
14.4
14.6
14.8
15.0
t (ns)
c)
a_n (µm)
6
4
2
0
-2
-4
-6
14.2
14.4
14.6
14.8
15.0
15.2
15.4
t (ns)

Figure 15